

# DNA-based nanoparticle tension sensors reveal that T-cell receptors transmit defined pN forces to their antigens for enhanced fidelity

Yang Liu<sup>a</sup>, Lori Blanchfield<sup>b</sup>, Victor Pui-Yan Ma<sup>a</sup>, Rakieb Andargachew<sup>b</sup>, Kornelia Galior<sup>a</sup>, Zheng Liu<sup>a</sup>, Brian Evavold<sup>b</sup>, and Khalid Salaita<sup>a,c,1</sup>

<sup>a</sup>Department of Chemistry, Emory University, Atlanta, GA 30322; <sup>b</sup>Department of Microbiology and Immunology, Emory University School of Medicine, Atlanta, GA 30322; and <sup>c</sup>Wallace H. Coulter Department of Biomedical Engineering, Georgia Institute of Technology and Emory University, Atlanta, GA 30332

Edited by K. Christopher Garcia, Stanford University, Stanford, CA, and approved March 25, 2016 (received for review January 5, 2016)

T cells are triggered when the T-cell receptor (TCR) encounters its antigenic ligand, the peptide-major histocompatibility complex (pMHC), on the surface of antigen presenting cells (APCs). Because T cells are highly migratory and antigen recognition occurs at an intermembrane junction where the T cell physically contacts the APC, there are long-standing questions of whether T cells transmit defined forces to their TCR complex and whether chemomechanical coupling influences immune function. Here we develop DNA-based gold nanoparticle tension sensors to provide, to our knowledge, the first pN tension maps of individual TCR-pMHC complexes during T-cell activation. We show that naïve T cells harness cytoskeletal coupling to transmit 12–19 pN of force to their TCRs within seconds of ligand binding and preceding initial calcium signaling. CD8 coreceptor binding and lymphocyte-specific kinase signaling are required for antigen-mediated cell spreading and force generation. Lymphocyte function-associated antigen 1 (LFA-1) mediated adhesion modulates TCR-pMHC tension by intensifying its magnitude to values >19 pN and spatially reorganizes the location of TCR forces to the kinapse, the zone located at the trailing edge of migrating T cells, thus demonstrating chemomechanical crosstalk between TCR and LFA-1 receptor signaling. Finally, T cells display a dampened and poorly specific response to antigen agonists when TCR forces are chemically abolished or physically “filtered” to a level below ~12 pN using mechanically labile DNA tethers. Therefore, we conclude that T cells tune TCR mechanics with pN resolution to create a checkpoint of agonist quality necessary for specific immune response.

T-cell receptor | mechanotransduction | antigen discrimination | cell migration | molecular tension sensor

T-cell activation is a crucial step in adaptive immunity, offering defense against pathogens and cancer (1). During activation, the T-cell receptor (TCR) recognizes and binds to its ligand, the antigenic peptide-major histocompatibility complex (pMHC), which is expressed on the surface of antigen-presenting cells (APCs). Because T cells are continuously moving and scanning the surfaces of APCs for evidence of antigens, and TCR-ligand binding occurs at the junction between two cells, it is likely that the TCR experiences mechanical forces during normal T-cell function. Therefore, important questions in this area pertain to whether the TCR-pMHC complex experiences defined forces during T-cell activation, and whether these forces influence immune function (2).

An elegant body of single-molecule experiments further underscores the connection between TCR signaling and mechanics. For example, Lang and Reinherz (3) used optical tweezers to demonstrate that the TCR responds to physical forces applied using an optically trapped bead. This team also showed that the TCR undergoes distinct structural transitions within its FG loop (a region formed by F and G strands) when the pMHC-TCR complex is strained at ~15 pN (4). Complementary single-molecule force spectroscopy measurements using the biomembrane force probe by Zhu and Evavold (5) showed that the average TCR-pMHC bond lifetime

( $1/k_{\text{off}}$  rate) is enhanced when ~10 pN of tension is applied through a specific antigen. Enhancement of bond lifetime under the influence of antigen mechanical strain (~10 pN) was further demonstrated in CD4<sup>+</sup> T cells (6) and for pre-TCR-pMHC interactions (7). These experiments specifically demonstrate an inherent TCR sensitivity to pN forces transmitted through its cognate pMHC ligand (3–8).

The role of forces in modulating bond lifetimes is particularly striking given that the most widely accepted model of TCR activation invokes a kinetic proofreading mechanism, emphasizing the importance of the TCR-pMHC dissociation rate in boosting antigen specificity (2, 9). The implicit model is that a T cell actively regulates forces transmitted to its TCR-pMHC complex to fine-tune bond lifetimes, thereby enhancing selective and differential levels of TCR activation and regulating antigen discrimination and T-cell selection.

The role of mechanics in T-cell activation remains controversial, however. For example, does the T cell itself transmit 10–15 pN of tension to its engaged TCR-pMHC complex during the early stages of antigen proofreading? Although traction force microscopy methods demonstrate that T cells generate contractile forces ~5 min after activation (10, 11), there is no evidence showing that the TCR-pMHC complex experiences pN forces during initial antigen encounters. Such forces are beyond the spatial and temporal resolution of traction force microscopy. Therefore, new molecular approaches are needed to investigate intrinsic TCR mechanics and to determine the physical basis and physiological consequences of mechanics in immunology.

## Significance

**T cells protect the body against pathogens and cancer by recognizing specific foreign peptides on the cell surface. Because antigen recognition occurs at the junction between a migrating T cell and an antigen-presenting cell (APC), it is likely that cellular forces are generated and transmitted through T-cell receptor (TCR)-ligand bonds. Here we develop a DNA-based nanoparticle tension sensor producing the first molecular maps of TCR-ligand forces during T cell activation. We find that TCR forces are orchestrated in space and time, requiring the participation of CD8 coreceptor and adhesion molecules. Loss or damping of TCR forces results in weakened antigen discrimination, showing that T cells harness mechanics to optimize the specificity of response to ligand.**

Author contributions: Y.L., B.E., and K.S. designed research; Y.L., L.B., V.P.-Y.M., K.G., and Z.L. performed research; Y.L., L.B., V.P.-Y.M., R.A., B.E., and K.S. analyzed data; and Y.L., L.B., B.E., and K.S. wrote the paper.

The authors declare no conflict of interest.

This article is a PNAS Direct Submission.

<sup>1</sup>To whom correspondence should be addressed. Email: k.salaita@emory.edu.

This article contains supporting information online at [www.pnas.org/lookup/suppl/doi:10.1073/pnas.1600163113/-DCSupplemental](http://www.pnas.org/lookup/suppl/doi:10.1073/pnas.1600163113/-DCSupplemental).

## Results

**Fabrication and Characterization of the DNA-Based Nanoparticle Tension Sensors.** We have developed an improved type of fluorescent tension probe to directly image and quantify the innate forces mediated by individual TCR complexes on ligand binding (Fig. 1A and *SI Appendix, Fig. S1*). These probes provide unprecedented sensitivity (*SI Appendix, Supplementary Note 1*), generating a  $\sim 100$ -fold fluorescence increase in response to pN forces (Fig. 1B and *SI Appendix, Fig. S2*). This sensitivity is essential given the transient nature and the limited number of TCR-pMHC antigens sufficient to activate T cells (12, 13). In brief, each tension probe consists of a DNA hairpin labeled with a fluorophore-quencher pair, and is immobilized onto a gold nanoparticle (AuNP). The mean interparticle spacing is  $48 \pm 8$  nm (Fig. 1C), which is physiologically optimal for antigen-mediated T-cell adhesion and functional responses (14, 15). Each particle presents an average of  $4 \pm 1$  DNA hairpins (*SI Appendix, Fig. S3*). The fluorophore is dual-quenched by both the molecular quencher through fluorescence resonance energy transfer (FRET) and the plasmon of the AuNP via nanometal surface energy transfer (NSET) pathway, thus reducing the background signal and boosting sensitivity over conventional molecular tension sensors (16–22). DNA hairpins generate fluorescence when the applied force exceeds the unfolding force,  $F_{1/2}$  (defined as the force at equilibrium for which a hairpin has a 50% probability of unfolding). Note that the probability of mechanical unfolding depends on the loading rate and the duration of the force, and thus the reported  $F_{1/2}$  values serve as a lower bound of the applied force given that the physiological loading rates and bond lifetimes are unknown. Importantly, the  $F_{1/2}$  can be tuned from  $\sim 2.4$  to 19.0 pN through the GC content and stem-loop structure of the hairpin (23) (*SI Appendix, Table S1*). Each probe exclusively responds to forces transmitted through a single TCR molecule (*SI Appendix, Fig. S4*).

**Piconewton Forces Are Transmitted by Individual TCR Complexes Before T-Cell Activation.** As a proof of concept, we used anti-CD3 antibody ( $\alpha$ -CD3)-modified probes ( $F_{1/2} = 19$  pN) to map TCR forces during the activation of naïve OT-1 cells (Fig. 1D and *Movie S1*), with  $F_{1/2}$  determined at 23 °C (*SI Appendix, Supplementary Note 2*). T cells began to spread within seconds of encountering the  $\alpha$ -CD3 ligand surface, and then continued to spread up to  $\sim 8$ –10  $\mu$ m in diameter. A punctate 19-pN tension signal was generated within seconds of initial surface contact and progressively increased thereafter, becoming enriched at the periphery of the contact area in a ring-like pattern. This result provides, to our knowledge, the first demonstration that the T cell innately transmits pN forces to its TCR complex in a defined spatial and temporal pattern.

Simultaneous tracking of TCR triggering using a ratiometric fura-2  $\text{Ca}^{2+}$  indicator showed that the initial appearance of forces preceded the rise in  $[\text{Ca}^{2+}]$  by  $35 \pm 15$  s (Fig. 1D, E, and G;  $n = 20$  cells). The initial  $\text{Ca}^{2+}$  flux was observed  $\sim 1$  min after initial cell contact, and peaked at  $\sim 2$  min (Fig. 1F). Interestingly, the tension signal continued to rise even after the initial  $\text{Ca}^{2+}$  flux started to subside, with a  $400 \pm 30$  s delay between the maximum  $[\text{Ca}^{2+}]$  and the maximum TCR tension signals (Fig. 1F and H;  $n = 20$  cells). Therefore, initial TCR triggering is tightly associated with its mechanics, and downstream signaling, such as  $\text{Ca}^{2+}$  flux, further amplifies TCR forces.

Although several lines of evidence demonstrate that actin-mediated cytoskeleton dynamics are crucial in T-cell biomechanics (24–26), the cytoskeletal factors that specifically initiate the rise of TCR-ligand forces remain unclear. To address this question, we treated naïve OT-1 cells with a library of cytoskeletal inhibitors and measured cell spreading and TCR-ligand forces (*SI Appendix, Fig. S5*). The GTPase Cdc42 was identified as critical to initiating the rise of TCR-ligand forces. Myosin light chain kinase and Arp2/3 were found to be important in maintaining TCR-ligand forces, and their inhibition caused drastic cell retraction and ring-shaped condensation

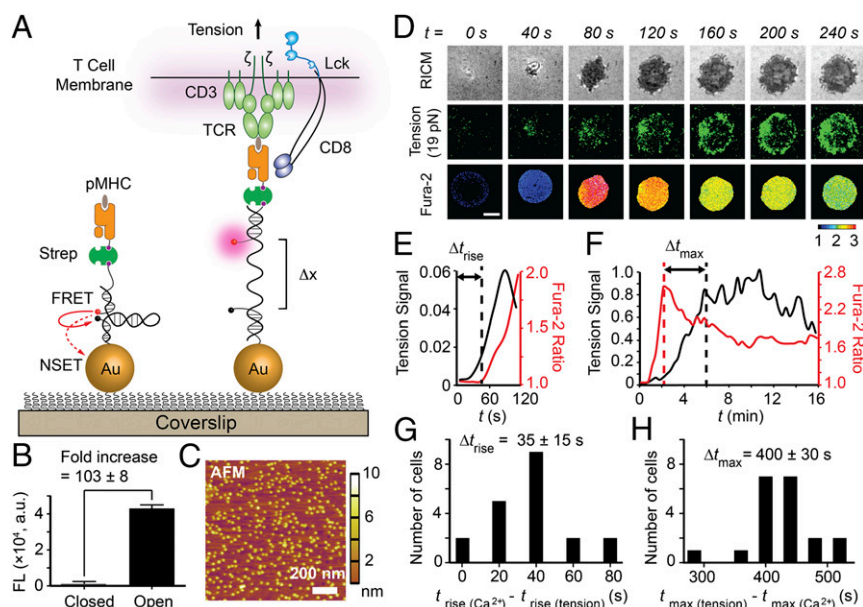


**Fig. 1.** T cells apply pN forces to the TCR preceding the rise in  $\text{Ca}^{2+}$ . (A) Schematic of DNA-based AuNP sensor for mapping TCR-mediated tension. The fluorescence of the Cy3B dye (pink dot) is dequenched on mechanical unfolding of the hairpin, which separates the dye from the black hole quencher 2 (BHQ2, black dot) and AuNP surface ( $\Delta x \approx 16.9$  nm). (B) Plot showing the fluorescence intensity of the closed and open forms of the hairpin. There is a  $103 \pm 8$ -fold increase in fluorescence on the opening of hairpins.  $n = 3$ . Error bars indicate SD. (C) AFM image showing the immobilized AuNP sensors on a glass coverslip. (D) Simultaneous imaging of cell spreading (RICM), 19 pN TCR forces (tension), and T-cell activation (fura-2) for a representative OT-1 cell encountering  $\alpha$ -CD3 antigen. Unless noted otherwise, all experiments were performed at 23 °C, the temperature at which  $F_{1/2}$  values were determined experimentally. (Scale bar: 3  $\mu$ m.) (E and F) Representative plots of tension signal and fura-2 ratio showing temporal differences between the initial rise of  $[\text{Ca}^{2+}]$  and the initial rise in TCR tension ( $\Delta t_{\text{rise}}$ ) and between the maximum  $[\text{Ca}^{2+}]$  and the maximum TCR tension signal ( $\Delta t_{\text{max}}$ ), and for the cell shown in D. The normalized y-axis applies to E and F. (G and H) Histogram analysis of  $\Delta t_{\text{rise}}$  and  $\Delta t_{\text{max}}$  ( $n = 20$  cells).



of tension signals (Movie S2). This result mirrors the disruptive reorganization of F-actin after blebbistatin and jaspalakinolide treatment of Jurkat cells, where actin retrograde flow is hypothesized to exert pushing and pulling forces (25). Furthermore, immunostaining showed that TCR forces highly colocalized with F-actin and were further surrounded by a slightly inward ring pattern of myosin light chain kinase (SI Appendix, Fig. S6). This is consistent with the actomyosin-enriched contraction arc in the lamella (25). Therefore, TCR-ligand forces are highly regulated by precise coordination between actin dynamics and actomyosin contractility.

**TCR-Ligand Tension Requires Coreceptor Engagement and Is Modulated by Adhesion Molecules.** We next aimed to define the magnitude of innate T-cell forces transmitted through the TCR-pMHC bond. For this, we used two DNA tension probes with  $F_{1/2} = 12$  pN or 19 pN and monitored hairpin unfolding in response to the wild-type N4 ligand, the most potent of the ovalbumin (OVA) antigenic ligands (Fig. 2A). After naïve OT-1 T lymphocytes engaged the surface for 15 min, the cells generated a strong tension signal on the 12-pN probe surface. In contrast, OT-1 T cells failed to unfold the 19-pN sensor (N4 antigen) despite fully spreading on this surface, as determined by reflection interference contrast microscopy (RICM). Because shear flow is known to generate TCR forces (27), we applied external flow to cells immobilized through the 19-pN probe (with N4 antigen), and observed a rapid and robust increase in tension signal (SI Appendix, Fig. S7). This experiment demonstrates that the pMHC-TCR bond can withstand forces >19 pN in the presence of CD8 coreceptor, but the innate TCR forces fall within

the 12–19 pN range. Thus, TCR mechanics are precisely tuned with an accuracy of a few  $\sim$ kcal/mol.

To determine the characteristic time course of initiation of TCR-pMHC forces, we next imaged the surface immediately after culture of naïve OT-1 cells onto 12-pN tension probes. The T cells generated punctate fluorescence tension signal within 40 s of cell-surface contact (Fig. 2B and Movie S3). This tension signal increased in intensity and spread until it reached a steady state, coinciding with cell spreading as determined by the RICM channel. Spatial analysis at  $t = 2$  min showed that forces were generally concentrated in a ring-like structure 1–2  $\mu$ m wide at the cell periphery (SI Appendix, Fig. S8). This ring-like distribution was short-lived, however, becoming diffuse across the junction at 2–5 min after cell-surface contact. Subsequently (>5 min), tension was enriched at the center of the contact zone, reminiscent of the central supramolecular activating cluster (28).

We further analyzed the spatial colocalization between tension, TCR, CD8 (coreceptor), and lymphocyte-specific kinase (Lck), which is essential for T-cell activation (29, 30). In contrast to the tension signal near the cell edge, TCRs were distributed uniformly across the cell-substrate interface (Fig. 2C). Therefore, the T cell applies force only to a subset of its TCRs. Notably, CD8 also was distributed homogeneously across the cell membrane, whereas phosphorylated (active) Lck (pY394) was highly colocalized with TCR tension (Pearson correlation =  $0.84 \pm 0.04$ ;  $n = 20$  cells) (Fig. 2C and SI Appendix, Fig. S9), further supporting the relationship between mechanics and early signaling. To probe this relationship, we treated T cells with a Lck-specific inhibitor (31) before and after cell plating (SI Appendix, Fig. S10). Inhibition of Lck after cell plating led to an  $\sim$ 20–30% reduction in tension signals, whereas

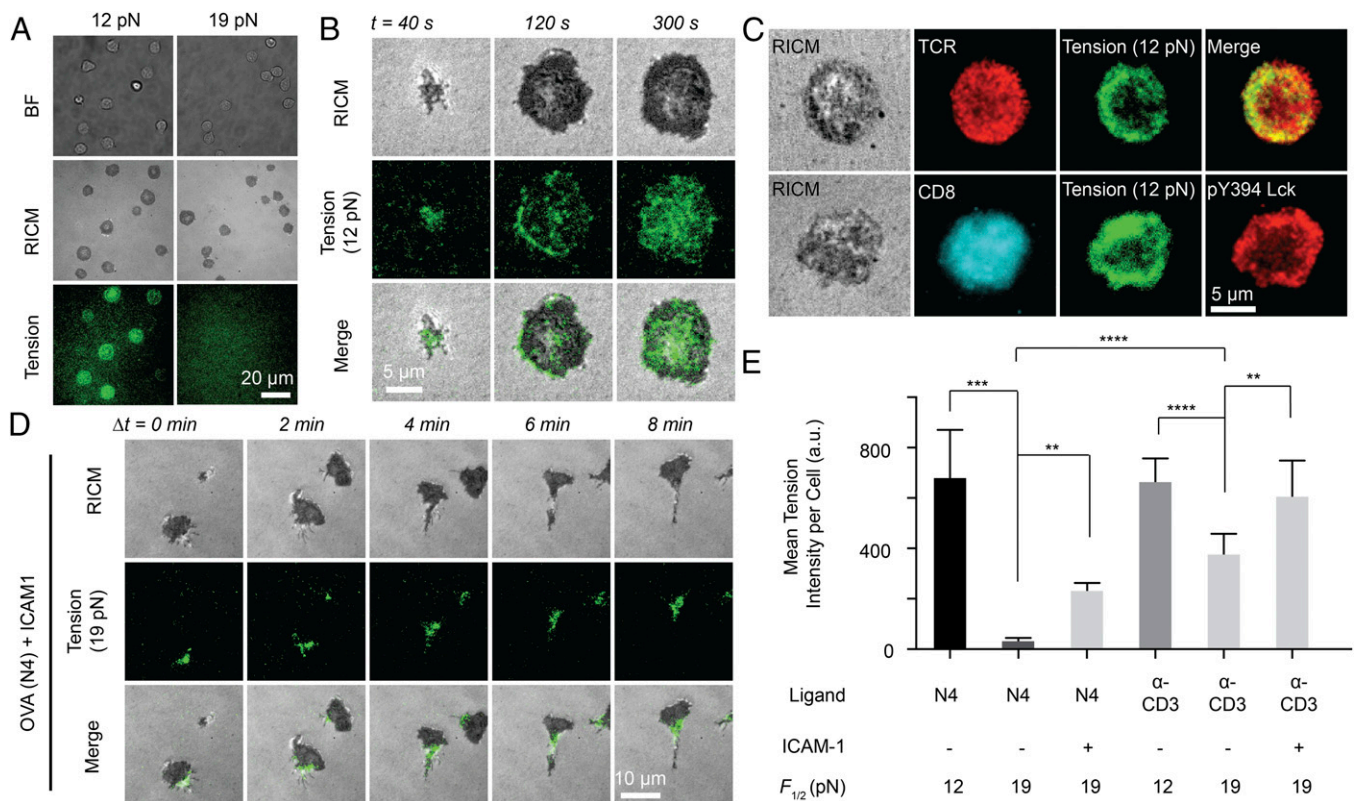


**Fig. 2.** Magnitude and spatial organization of TCR-antigen forces are highly dependent on antigen and adhesion receptor binding. (A) Representative bright-field, RICM, and tension (12 pN and 19 pN) images of OT-1 cells cultured on tension probe surfaces modified with N4 pMHC. (B) Representative RICM and tension (12 pN) images taken from a time-lapse movie for an OT-1 cell on N4 ligand stimulation (Movie S3). (C) Representative immunostaining images showing colocalization between TCR and 12 pN tension (Upper) and colocalization among active Lck (pY394), CD8, and 12 pN TCR tension (Lower) at  $t = 5$  min. (D) Representative RICM and 19 pN TCR tension images taken from a time-lapse movie for an OT-1 cell on N4 and ICAM-1 stimulation (Movie S4). (E) Bar graph showing the TCR tension intensity on ligand stimulation with N4,  $\alpha$ -CD3, and ICAM-1.  $n = 20$  cells. Error bars represent SD. \*\* $P < 0.01$ ; \*\*\* $P < 0.001$ ; \*\*\*\* $P < 0.0001$ .

pretreatment with Lck inhibitor abolished tension and cell spreading. This abolishment was also achieved by antibody blocking of the CD8 coreceptor or with a mutant pMHC that inhibits coreceptor binding (*SI Appendix, Fig. S10*). Therefore, the generation of TCR forces  $>12$  pN requires CD8 coreceptor and its associated Lck.

TCR-pMHC binding is the first step in the TCR triggering cascade that includes a variety of ligand-receptor pairs during T cell-APC contact. For example, adhesion receptors such as LFA-1 and other costimulatory receptors also bind to their ligands at the intercellular junction, which has been proposed to modulate TCR-pMHC forces (32). A binary surface copresenting ICAM-1 ligands and the N4 ligands was engineered using orthogonal chemistry such that TCR forces were exclusively visualized and quantified through the N4 antigen and without convolution from adhesion-mediated forces (Fig. 2*D* and *SI Appendix, Fig. S11*). Our results show that the incorporation of ICAM-1 not only led to enhanced TCR forces beyond 19 pN, but also triggered a profound change in T-cell morphology and motility. Shortly after engaging the surface (1–5 min), OT-1 cells polarized, forming a kinapse structure that coincided with cell migration at velocities of  $\sim 1$ – $2$   $\mu\text{m}/\text{min}$  (*Movie S4*). TCR forces were observed primarily at the trailing edge (focal zone) of the T cell, in agreement with a recent model integrating cell motility (surveillance) and TCR signaling (33, 34). Fig. 2*E* summarizes the average TCR forces with N4 and  $\alpha$ -CD3 ligands, as well as the role of ICAM-1 in modulating this force ( $n = 20$  cells per group). These data unambiguously show that TCR forces are regulated by antigen and adhesion ligand engagement.

### T Cells Harness Mechanical Forces as a Checkpoint of Antigen Quality.

A key property of T cells is their ability to differentiate nearly identical pMHC ligands with distinct levels of response (35, 36). We

asked whether TCR mechanics contribute to the specificity of its response to antigen. To answer this question, we used the less potent ligands Q4 and V4, differing by single amino acid mutations at the fourth position (36) and compared tension signals with that of the OVA N4 antigen. As an initial test, time-lapse imaging showed that the TCR mechanically interrogates the less potent V4 ligand with  $>12$  pN forces, albeit at differing time scales (*SI Appendix, Fig. S12A* and *Movie S5*). TCR-pMHC forces were more transient and punctate for V4, in contrast to the greater mechanical response to N4 ligand (*SI Appendix, Fig. S12B* and *Movie S6*). Moreover, the delay between the rise in  $[\text{Ca}^{2+}]$  and the rise in tension exceeded 5 min for V4, further confirming that TCR-pMHC mechanics are associated with early antigen discrimination.

To relate TCR mechanics with T-cell functional response, we plated naïve OT-1 cells onto 12-pN tension sensors displaying N4, Q4, and V4 OVA pMHCs as well as  $\alpha$ -CD3. Simultaneously, we measured T-cell activation by quantifying the immunofluorescence of Zap70 phosphorylation (pY319) when Cdc42-mediated tension was chemically inhibited and compared it with the value in the DMSO control (Fig. 3*A*). The tension signal and ligand potency decreased from  $\alpha$ -CD3 to N4, Q4, and V4 (Fig. 3*B* and *C*, red bars). Ligand potency was consistent with literature values determined using IFN- $\gamma$  production (36). When the Cdc42 inhibitor (ML141) was used, there were marked reductions in TCR tension and T-cell activation (Fig. 3*B* and *C*, blue bars). Plotting the total TCR tension against Zap70 phosphorylation showed a strong correlation (Fig. 3*D*; Pearson correlation = 0.99), further supporting a strong relationship between TCR tension and T-cell activation. Importantly, the range of T-cell responses are dampened on Cdc42 inhibition, indicating that TCR tension and ligand discrimination are related.

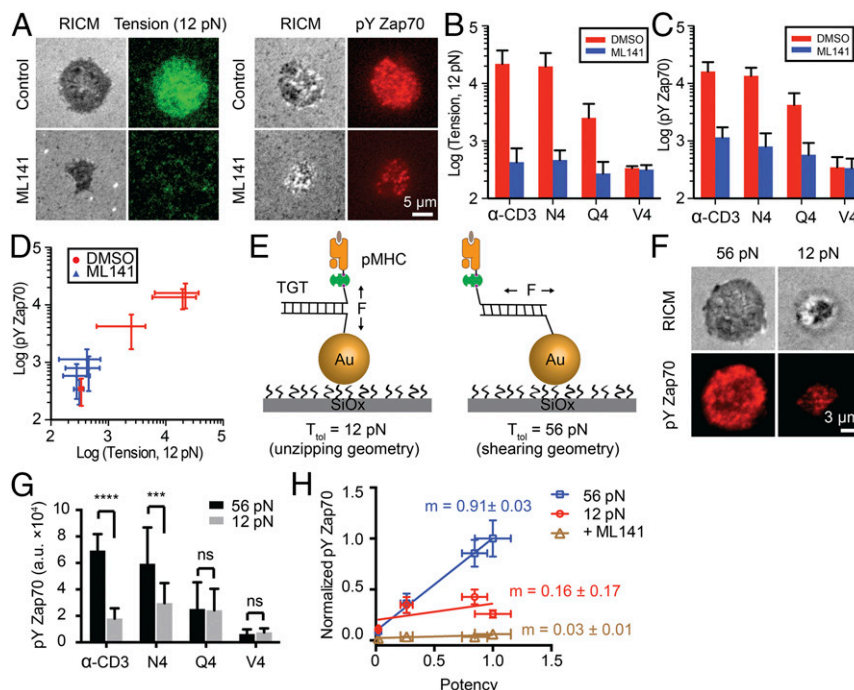


**Fig. 3.** TCR forces enhance antigen specificity. (A) Representative images showing TCR tension and pYZap70 on N4 stimulation with or without ML141 treatment for 30 min. (B and C) Bar graphs quantifying TCR tension signals (B) and pYZap70 staining levels (C) for single OT-1 cells on ligand stimulation with  $\alpha$ -CD3, N4, Q4, and V4 antigens.  $n = 20$  cells for each group. Error bars represent SD. (D) Plot showing the correlation between TCR tension signal and pYZap70 levels for different ligands. (E) Schematic showing TGTs for modulating TCR forces and T-cell activation. TGTs in an unzipping mode (12 pN) or in a shearing mode of TGT (56 pN) were immobilized onto the 9-nm AuNP through an Au-thiol interaction. Different ligands were conjugated to the TGTs through biotin-streptavidin binding. (F) Representative images showing differential T-cell activation on N4 pMHC-modified 12 pN TGT compared with the 56 pN TGT. (G) Bar graph showing pYZap70 levels on stimulation with pMHCs anchored through the 12 or 56 pN TGT at 37  $^{\circ}\text{C}$ .  $n = 20$  cells for each group. Error bars represent SD.  $***P < 0.001$ ;  $****P < 0.0001$ . (H) Plot of pYZap70 levels in response to ligands with increasing potency. The slope ( $m$ ) indicates the T-cell specificity to different ligands.  $n = 20$  cells from triplicate measurements. Error bars represent SEM.



We next adapted the recently reported DNA tension gauge tether (TGT) (37, 38) into our AuNP platform to physically modulate TCR forces (Fig. 3E). The TGT is a DNA duplex tailored to dissociate at force levels that exceed its mechanical tolerance,  $T_{\text{tol}}$  (defined as the rupture force when a constant force is applied for 2 s). In this way, the chemical recognition (affinity) between the TCR and antigenic ligand is maintained; however, the TGT sets the upper limit of forces experienced between a cell-surface receptor and its ligand. Given that TCR forces are in the range of 12–19 pN for the N4 antigen (Fig. 2E), we designed ligands anchored through previously validated TGTs with  $T_{\text{tol}}$  values of 56 pN and 12 pN (SI Appendix, Table S1), which provide the largest possible difference in mechanical resistance ( $T_{\text{tol}}$  determined at 37 °C) (SI Appendix, Supplementary Note 2). Indeed, the 12-pN TGT presenting  $\alpha$ -CD3 displayed greater dissociation compared with the 56-pN TGT (SI Appendix, Fig. S13). After culturing naïve OT-1 cells for 30 min onto the 12 pN and 56 pN TGT surfaces decorated with N4, Q4, and V4 OVA pMHCs as well as  $\alpha$ -CD3, T-cell activation was quantified using pYZap70 (pY319) (Fig. 3 F and G). Note that all TGT experiments were performed at 37 °C, the temperature at which  $T_{\text{tol}}$  values were determined.

Interestingly, the most potent ligands,  $\alpha$ -CD3 and N4, displayed the greatest pYZap70 levels when tethered through the 56-pN TGT, with a significant reduction in activation for the 12-pN TGT. Thus, more potent ligands display enhanced T-cell triggering by a pulling force >12 pN. The less potent Q4 and V4 antigens did not show a differential response to force (Fig. 3G). Therefore, T-cell activation levels are sensitive to the amount of self-generated force transmitted to the different TCR-pMHC bonds, allowing for the optimal (i.e., more potent) ligands to selectively benefit from intensified mechanical tension. With the 12-pN TGT, ligand potency is statistically similar across the different antigens. Capping the TCR-pMHC force to 12 pN likely leads to dampening differences in TCR-pMHC dwell times (39). When the cell is allowed to intensify TCR-pMHC tension before it dissociates, the tested ligands further resolve with different levels of pYZap70 and functional responses. This is shown graphically by plotting the pYZap70 levels against ligand potency (Fig. 3H). Taken together, these experiments demonstrate that cell-generated forces transmitted to the TCR-pMHC bond amplify the specificity of antigen recognition, which is a required feature of T-cell function.

## Discussion

We imaged TCR forces with the highest spatial and temporal resolution reported to date using improved molecular tension sensors. We reveal that naïve T cells generate forces in the 12–19 pN range during initial antigen recognition (Fig. 2 and SI Appendix, Fig. S12). Importantly, our results complement and further validate the physiological relevance of a significant body of single-molecule measurements showing that external forces, in the ~10–20 pN range, drive structural transitions in the TCR and enhance the TCR-pMHC bond lifetime for strong agonists (4, 5, 7). It is no coincidence that the T cell strains its TCR-pMHC complex to tension values similar to those that achieve maximal “catch bond” behavior (a counterintuitive enhancement in bond lifetime that occurs when a bond experiences mechanical strain), as determined in single-molecule experiments.

Our results also suggest that agonists, both strong and weak, experience a pN mechanical stringency test, but strong agonists selectively display enhanced activation, presumably owing to enhanced bond lifetime. T cells harness mechanical forces to aid discrimination between strong and weak agonists by inducing differential phosphorylation levels of Zap70 (Fig. 3), further supporting the force-dependent mechanisms of T-cell activation (40). Given that LFA-1 engagement is not required to generate TCR-pMHC tension, mechanical testing of antigen seems to be independent of T-cell migration processes.

Our data also point to a dual role for mechanics in T-cell function (Fig. 4). First, TCR-pMHC forces are involved in initial ligand discrimination as a fidelity checkpoint. As discussed above, T cells likely harness mechanics to maximize the TCR-pMHC bond lifetime for cognate ligands. Second, following T-cell triggering and  $\text{Ca}^{2+}$  flux, myosin contractility is enhanced, further mounting TCR forces and leading to cell spreading. This in turn increases the number of TCR-pMHC engagements at the T cell-APC junction by simply flattening the cell-cell interface (Fig. 4A). This chemomechanical feedback maximally amplifies the distinct TCR signaling levels between strong and weak agonists, demonstrating a mechanically regulated model for antigen discrimination (Fig. 4 B and C).

By decorating the tension sensor with different ligands, we have shown that the magnitude of TCR forces are significantly lower in response to cognate N4 antigen compared with the  $\alpha$ -CD3 ligand (Fig. 2). This conclusion is not simply a result of selective bond rupture; rather, T cells transmit defined forces to a subset of engaged receptors (SI Appendix, Fig. S7). These data suggest the existence of a self-regulatory mechanism for the fine-tuning of force generation. The observations that CD8 binding and Lck kinase activity are essential in mediating force generation (SI Appendix, Fig. S10) suggest chemical mechanisms of force regulation.

LFA-1/ICAM-1 binding results in a migratory phenotype of OT-1 cells and also generates a higher level of TCR-pMHC tension within the focal zone (Fig. 2 D and E and Movie S4), where adhesion molecules including CD2 (41), talin (42) and Rho-associated kinase (43) are enriched. Our data support the emerging motile

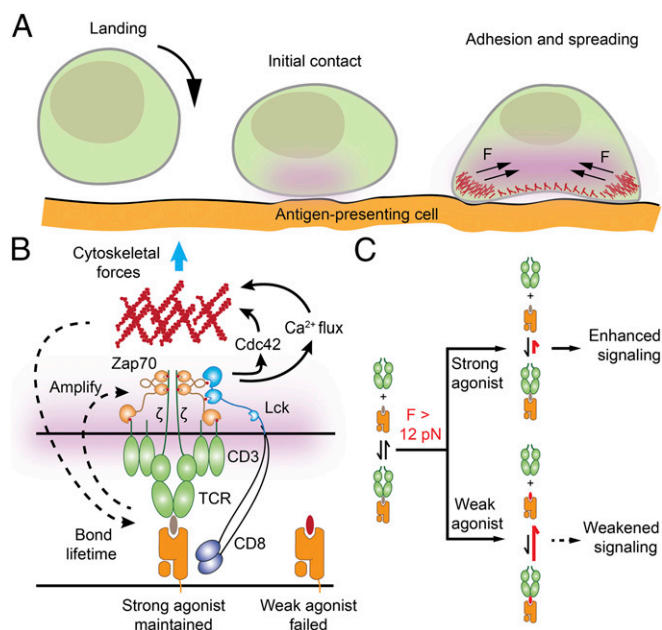


**Fig. 4.** Proposed model for T-cell force generation and antigen discrimination. (A) Initial ligand-receptor engagement occurs when a T cell physically encounters an antigen-presenting cell. If strong pMHC agonists are encountered, the TCR is triggered and the initial signal is amplified, leading to cell adhesion, spreading, and force enhancement. (B) Speculative model depicting how T cells harness a chemomechanical feedback mechanism to increase the specificity of TCR signaling and distinguish between strong and weak agonists. The chemical triggering of TCR activates cytoskeletal processes that further enhance mechanical testing of the TCR-pMHC bond. (C) Data showing that TCR-pMHC complexes experience tension >12 pN during initial ligand-receptor sampling and engagement. Moreover, TCR-pMHC forces >12 pN lead to greater levels of downstream signaling for strong agonists compared with the levels achieved through weaker agonists. The mechanism of differential response to force is likely through catch bond behavior, as shown by Liu et al. (5).

synapse model in migratory OT-1 cells (33) and further demonstrate active crosstalk between TCR signaling and LFA-1 activation. Because T-cell migration relies on LFA-1 mediated detachment of the trailing edge (focal zone), our observation points to an idea that TCR signaling is coupled to and modulated by mechanics in the kinapse during lymphocyte surveillance and immune function.

Finally, our method provides, to our knowledge, the first platform for decoupling the specific forces transmitted through the TCR from those forces mediated by LFA-1/ICAM-1 interactions (Fig. 2D, *SI Appendix*, Fig. S11, and *Movie S4*). In principle, the high modularity of the method should permit a generalization to investigate the mechanics of any specific surface receptors in the context of other intercellular interactions (e.g., receptor–ligand and glycan–glycan interactions), which normally show synergistic effects at the cellular level. This design of a molecular tension sensor better resembles the complex nature of cell–cell junctions and provides a readout of mechanics with molecular specificity that is beyond the capabilities of conventional traction force microscopy and single-molecule force spectroscopy methods.

## Materials and Methods

**DNA Labeling.** A mixture of A21B (10 nmol) and excess Cy3B NHS ester in 0.1 M sodium bicarbonate solution was allowed to react at room temperature overnight. The mixture was then subjected to P2 gel filtration to remove salts, organic solvent, and unreacted reactants, and further purified by reverse-

phase HPLC (solvent A: 0.1 M TEAA; solvent B: 100% MeCN); the initial condition was 10% B with a gradient of 1%/min and a flow rate of 1 mL/min. The desired product was characterized by MALDI-TOF mass spectrometry.

**Optical Microscopy.** Live cells were imaged in Hank's balanced salt imaging buffer at 23 °C. In the TGT experiments, cells were incubated in the imaging buffer at 37 °C for 30 min before fixation. The microscope was a Nikon Eclipse Ti driven by the Elements software package. The microscope featured an Evolve electron multiplying charge coupled device (Photometrics), an Intensilight epifluorescence source (Nikon), a CFI Apo 100× NA 1.49 objective (Nikon), and a TIRF launcher with three laser lines: 488 nm (10 mW), 561 nm (50 mW), and 638 nm (20 mW). This microscope also included the Nikon Perfect Focus System, an interferometry-based focus lock that allowed the capture of multipoint and time-lapse images without loss of focus. All of the reported experiments were performed using the following Chroma filter cubes: TIRF 488, TIRF 640, TRITC, and RCM.

More detailed information about the materials and methods used in this study is provided in *SI Appendix, Materials and Methods*.

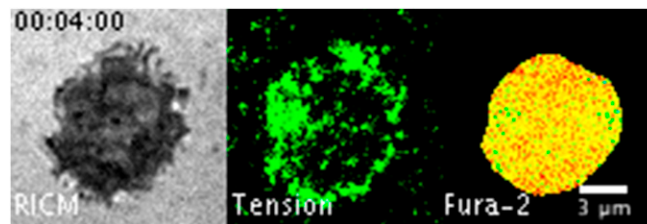
**ACKNOWLEDGMENTS.** We thank the National Institutes of Health (NIH) Tetramer Facility at Emory University for providing the biotinylated pMHC monomers. K.S. was supported by NIH Grant R01 GM097399, an Alfred P. Sloan Research Fellowship, a Camille Dreyfus Teacher-Scholar Award, and National Science Foundation CAREER Award 1350829. L.B. was supported by a postdoctoral fellowship from the National Multiple Sclerosis Society (FG1963A1/1). R.A. was supported by NIH Grant T32 AI007610. B.E. and R.A. were supported by NIH Grant R01 AI096879.

- Smith-Garvin JE, Koretzky GA, Jordan MS (2009) T cell activation. *Annu Rev Immunol* 27:591–619.
- Chakraborty AK, Weiss A (2014) Insights into the initiation of TCR signaling. *Nat Immunol* 15(9):798–807.
- Kim ST, et al. (2009) The alphabeta T cell receptor is an anisotropic mechanosensor. *J Biol Chem* 284(45):31028–31037.
- Das DK, et al. (2015) Force-dependent transition in the T-cell receptor  $\beta$ -subunit allosterically regulates peptide discrimination and pMHC bond lifetime. *Proc Natl Acad Sci USA* 112(5):1517–1522.
- Liu B, Chen W, Evavold BD, Zhu C (2014) Accumulation of dynamic catch bonds between TCR and agonist peptide MHC triggers T cell signaling. *Cell* 157(2):357–368.
- Hong J, et al. (2015) Force-regulated in situ TCR peptide-bound MHC class II kinetics determine functions of CD4<sup>+</sup> T cells. *J Immunol* 195(8):3557–3564.
- Mallis RJ, et al. (2015) Pre-TCR ligand binding impacts thymocyte development before  $\alpha\beta$ TCR expression. *Proc Natl Acad Sci USA* 112(27):8373–8378.
- Liu Z, et al. (2016) Nanoscale optomechanical actuators for controlling mechanotransduction in living cells. *Nat Methods* 13(2):143–146.
- McKeithan TW (1995) Kinetic proofreading in T-cell receptor signal transduction. *Proc Natl Acad Sci USA* 92(11):5042–5046.
- Bashour KT, et al. (2014) CD28 and CD3 have complementary roles in T-cell traction forces. *Proc Natl Acad Sci USA* 111(6):2241–2246.
- Hui KL, Balagopal L, Samelson LE, Upadhyaya A (2015) Cytoskeletal forces during signaling activation in Jurkat T-cells. *Mol Biol Cell* 26(4):685–695.
- Huppa JB, et al. (2010) TCR-peptide MHC interactions in situ show accelerated kinetics and increased affinity. *Nature* 463(7283):963–967.
- O'Donoghue GP, Pielak RM, Smoligovets AA, Lin JJ, Groves JT (2013) Direct single molecule measurement of TCR triggering by agonist pMHC in living primary T cells. *eLife* 2:e00778.
- Deeg J, et al. (2013) T cell activation is determined by the number of presented antigens. *Nano Lett* 13(11):5619–5626.
- Delcassian D, et al. (2013) Nanoscale ligand spacing influences receptor triggering in T cells and NK cells. *Nano Lett* 13(11):5608–5614.
- Liu Y, Yehli K, Narui Y, Salaita K (2013) Tension sensing nanoparticles for mechanotransduction at the living/nonliving interface. *J Am Chem Soc* 135(14):5320–5323.
- Liu Y, et al. (2014) Nanoparticle tension probes patterned at the nanoscale: Impact of integrin clustering on force transmission. *Nano Lett* 14(10):5539–5546.
- Zhang Y, Ge C, Zhu C, Salaita K (2014) DNA-based digital tension probes reveal integrin forces during early cell adhesion. *Nat Commun* 5:5167.
- Blakely BL, et al. (2014) A DNA-based molecular probe for optically reporting cellular traction forces. *Nat Methods* 11(12):1229–1232.
- Gallor K, Liu Y, Yehli K, Vivek S, Salaita K (2016) Titin-based nanoparticle tension sensors map high-magnitude integrin forces within focal adhesions. *Nano Lett* 16(1):341–348.
- Jurchenko C, Chang Y, Narui Y, Zhang Y, Salaita KS (2014) Integrin-generated forces lead to streptavidin-biotin unbinding in cellular adhesions. *Biophys J* 106(7):1436–1446.
- Chang Y, et al. (2016) A general approach for generating fluorescent probes to visualize piconewton forces at the cell surface. *J Am Chem Soc* 138(9):2901–2904.
- Woodside MT, et al. (2006) Nanomechanical measurements of the sequence-dependent folding landscapes of single nucleic acid hairpins. *Proc Natl Acad Sci USA* 103(16):6190–6195.
- Yu Y, Fay NC, Smoligovets AA, Wu HJ, Groves JT (2012) Myosin IIA modulates T cell receptor transport and Ca<sup>2+</sup> phosphorylation during early immunological synapse formation. *PLoS One* 7(2):e30704.
- Yi J, Wu XS, Crites T, Hammer JA, 3rd (2012) Actin retrograde flow and actomyosin II arc contraction drive receptor cluster dynamics at the immunological synapse in Jurkat T cells. *Mol Biol Cell* 23(5):834–852.
- Babich A, et al. (2012) F-actin polymerization and retrograde flow drive sustained PLC $\gamma$ 1 signaling during T cell activation. *J Cell Biol* 197(6):775–787.
- Li YC, et al. (2010) Cutting edge: Mechanical forces acting on T cells immobilized via the TCR complex can trigger TCR signaling. *J Immunol* 184(11):5959–5963.
- Grakoui A, et al. (1999) The immunological synapse: A molecular machine controlling T cell activation. *Science* 285(5425):221–227.
- Lee KH, et al. (2002) T cell receptor signaling precedes immunological synapse formation. *Science* 295(5559):1539–1542.
- Casas J, et al. (2014) Ligand-engaged TCR is triggered by Lck not associated with CD8 coreceptor. *Nat Commun* 5:5624.
- Hui E, Vale RD (2014) In vitro membrane reconstitution of the T-cell receptor proximal signaling network. *Nat Struct Mol Biol* 21(2):133–142.
- Beemiller P, Krummel MF (2010) Mediation of T-cell activation by actin meshworks. *Cold Spring Harb Perspect Biol* 2(9):a002444.
- Beemiller P, Jacobelli J, Krummel MF (2012) Integration of the movement of signaling microclusters with cellular motility in immunological synapses. *Nat Immunol* 13(8):787–795.
- Choudhuri K, et al. (2014) Polarized release of T-cell receptor-enriched microvesicles at the immunological synapse. *Nature* 507(7490):118–123.
- Evavold BD, Allen PM (1991) Separation of IL-4 production from Th cell proliferation by an altered T cell receptor ligand. *Science* 252(5010):1308–1310.
- Zehn D, Lee SY, Bevan MJ (2009) Complete but curtailed T-cell response to very low-affinity antigen. *Nature* 458(7235):211–214.
- Wang X, Ha T (2013) Defining single molecular forces required to activate integrin and notch signaling. *Science* 340(6135):991–994.
- Ma PV, et al. (2016) The mechanically-induced catalytic amplification reaction for readout of receptor-mediated cellular forces. *Angew Chem Int Ed* doi: 10.1002/anie.201600351.
- Klammt C, et al. (2015) T cell receptor dwell times control the kinase activity of Zap70. *Nat Immunol* 16(9):961–969.
- Depoil D, Dustin ML (2014) Force and affinity in ligand discrimination by the TCR. *Trends Immunol* 35(12):597–603.
- Tibaldi EV, Salgia R, Reinherz EL (2002) CD2 molecules redistribute to the uropod during T cell scanning: Implications for cellular activation and immune surveillance. *Proc Natl Acad Sci USA* 99(11):7582–7587.
- Smith A, et al. (2005) A talin-dependent LFA-1 focal zone is formed by rapidly migrating T lymphocytes. *J Cell Biol* 170(1):141–151.
- Smith A, Bracke M, Leitinger B, Porter JC, Hogg N (2003) LFA-1-induced T cell migration on ICAM-1 involves regulation of MLCK-mediated attachment and ROCK-dependent detachment. *J Cell Sci* 116(Pt 15):3123–3133.



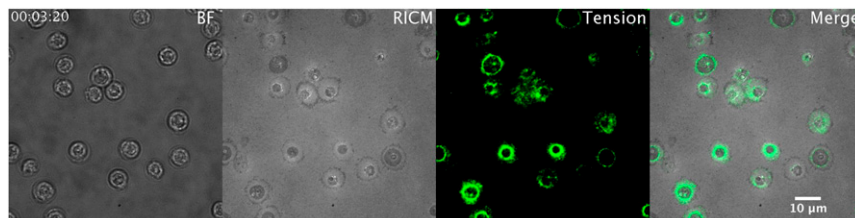
# Supporting Information

Liu et al. 10.1073/pnas.1600163113



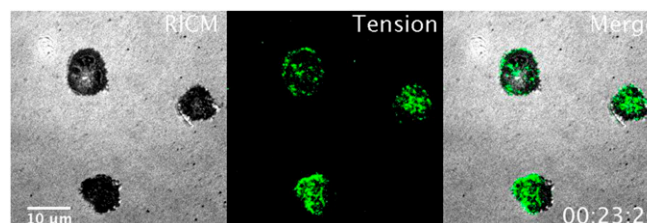
**Movie S1.** Simultaneous imaging of TCR tension generation and T-cell activation. Time-lapse video showing a naïve OT1 cell pretreated with fura-2 ratio-metric dye plated on a 19-pN tension probe substrate presenting  $\alpha$ -CD3. The video is 10 min long. The RISM channel (*Left*), TCR tension channel (*Middle*), and fura-2 ratio channel (*Right*) are shown side by side.

[Movie S1](#)



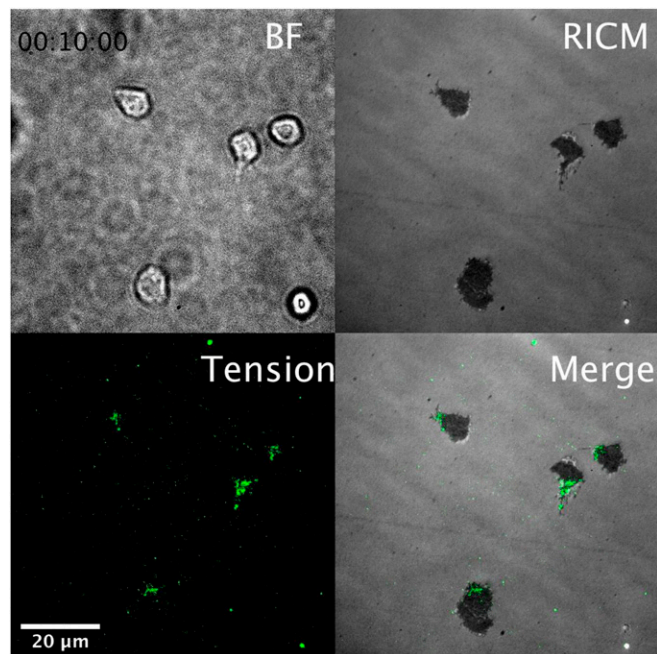
**Movie S2.** ML-7 leads to the shrinkage of cell-surface contact and condensation of tension. Time-lapse video showing naïve OT1 cells plated on a 12-pN tension probe substrate presenting N4 pMHC on treatment with 40  $\mu$ M of ML7.  $t = 0$  min represents the time at which ML7 was added. The bright-field channel, RISM channel, TCR tension channel, and merged channel from RISM and tension are shown from left to right.

[Movie S2](#)



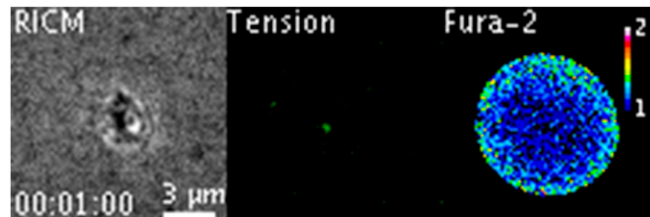
**Movie S3.** TCR tension dynamics in response to pMHC stimulation. Time-lapse video of naïve OT1 cells plated on a 12-pN tension probe substrate presenting N4 pMHC. The time-lapse movie was captured from  $t = 0$  min to  $t = 34$  min to show the spatiotemporal dynamics of TCR tension on cell-substrate contact. The RISM channel, TCR tension channel, and merged channel from RISM and tension are shown from left to right.

[Movie S3](#)



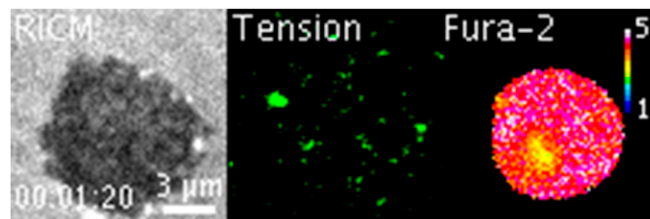
**Movie S4.** Cell migration and tension dynamics in response to the copresentation of pMHC/ICAM-1. Time-lapse video of naïve OT1 cells plated on a 19-pN tension probe substrate copresenting N4 pMHC and ICAM-1 ligands at 15 min after plating. The time-lapse movie was captured for 10 min to show the migratory behavior of T cells and characteristic TCR tension at the trailing edge. The interval between each frame is 30 s. The bright-field channel (*Top Left*), RICM channel (*Top Right*), TCR tension channel (*Bottom Left*), and merged channel from RICM and tension (*Bottom Right*) are shown in a quadrant.

[Movie S4](#)



**Movie S5.** OT-1 cell tension dynamics and  $[Ca^{2+}]$  flux in response to the V4 ligand. Time-lapse video of naïve OT1 cells pretreated with fura-2 ratiometric dye plated on a 12-pN tension probe substrate presenting V4 pMHC. The time-lapse movie is ~10 min long. The RICM channel (*Left*), TCR tension channel (*Middle*), and fura-2 ratio channel (*Right*) are shown side by side. The normalized fura-2 ratio is color-coded to represent values from 1.0 to 2.0.

[Movie S5](#)



**Movie S6.** OT-1 cell tension dynamics and  $[Ca^{2+}]$  flux in response to the N4 ligand. Time-lapse video of naïve OT1 cells pretreated with fura-2 ratiometric dye plated on a 12-pN tension probe substrate presenting N4 pMHC. The time lapse movie is ~6 min long. The RICM channel (*Left*), TCR tension channel (*Middle*), and fura-2 ratio channel (*Right*) are shown side by side. The normalized fura-2 ratio is color-coded to represent values from 1.0 to 5.0.

[Movie S6](#)



## Other Supporting Information Files

[SI Appendix \(PDF\)](#)

# Supporting information for

## DNA-based Nanoparticle Tension Sensors Reveal that T-cell Receptors Transmit Defined pN Forces to Their Antigens for Enhanced Fidelity

**Authors:** Yang Liu,<sup>1</sup> Lori Blanchfield,<sup>2</sup> Victor Pui-Yan Ma,<sup>1</sup> Rakieb Andargachew,<sup>2</sup> Kornelia Galior,<sup>1</sup> Zheng Liu,<sup>1</sup> Brian Evavold,<sup>2</sup> Khalid Salaita<sup>1,3\*</sup>

### Affiliations:

<sup>1</sup>Department of Chemistry, Emory University, Atlanta, GA 30322, USA

<sup>2</sup>Department of Microbiology and Immunology, Emory University School of Medicine, Atlanta, GA 30322, USA

<sup>3</sup>Wallace H. Coulter Department of Biomedical Engineering, Emory University and Georgia Institute of Technology, Atlanta, GA 30332, USA

\* Correspondence to: k.salaita@emory.edu

### This PDF file includes:

Materials and methods

Table S1 DNA sequences

Supplementary movie caption

Supplementary note 1 & 2

Fig. S1. Fabrication of DNA-based gold nanoparticle tension sensor surface

Fig. S2. Quenching efficiency calibration of DNA-AuNP tension probes

Fig. S3. Quantification of the average number of DNA sensors per gold nanoparticle

Fig. S4. Tension signals are specifically generated through TCR-ligand interaction

Fig. S5. Investigation of cytoskeletal elements mediating TCR forces

Fig. S6. Colocalization of TCR tension with F-actin, and F-actin with myosin light chain kinase

Fig. S7. Induction of 19 pN sensor by shear flow

Fig. S8. Radial distribution function analysis of TCR tension upon ligand stimulation

Fig. S9. Spatial correlation analysis between TCR tension and active Lck

Fig. S10. Quantification of TCR tension upon perturbation of TCR, CD8 and Lck activities

Fig. S11. Co-presentation of ICAM-1 and DNA tension sensor-pMHC ligands on AuNP

Fig. S12. Comparison of TCR forces and  $[Ca^{2+}]$  between V4 and N4 ligand

Fig. S13. Comparison of TGT rupturing between 12 pN and 56 pN probes



## **Materials and Methods**

### **Reagents**

(3-Aminopropyl) trimethoxysilane (97%, APTMS), triethylammonium acetate (TEAA), hank's balanced salts,  $\text{NiSO}_4 \cdot 6\text{H}_2\text{O}$ , Lck inhibitor (7-cyclopentyl-5-(4-phenoxyphenyl)-7H-pyrrolo[2,3-d]pyrimidin-4-ylamine), ROCK inhibitor (Y-27632), MLCK inhibitor (ML-7), F-actin inhibitor (Cytochalasin D), Arp2/3 inhibitor (CK-666), Rac1 inhibitor (NSC23766) were purchased from Sigma-Aldrich (St. Louis, MO) and used without further purification. Cdc42 inhibitor (ML141) was purchased from Santa Cruz Biotech (Dallas, Texas). The fluorescent dye Cy3B-NHS ester was purchased from GE healthcare Bio-Science (Pittsburgh, PA). Number two glass coverslips, ascorbic acid (>99.0%), and 96-well plates were purchased from Fisher Chemical & Scientific (Pittsburgh, PA). DMF (>99.5%), DMSO (99.5%) and sodium bicarbonate (99.0%) were purchased from EMD chemicals (Philadelphia, PA). P2 gel size exclusion beads were acquired from Biorad (Hercules, CA). Lipoic Acid-PEG-NHS (MW 3400) and mPEG-NHS (MW 2000) were purchased from Nanocs (New York, NY). NTA-SAM reagent was purchased from Dojindo (Rockville, Maryland). Recombinant mouse ICAM-1 Fc histag protein (catalog # 83550) was purchased from Biorbyt (San Francisco, CA). AuNPs were custom synthesized and characterized by TEM by Nanocomposix (San Diego, CA). Based on TEM analysis that was provided by the manufacturer, the mean diameter of these particles was  $8.6 \pm 0.6$  nm.

### **Antibodies**

Alexa fluor 647 conjugated anti-TCR antibody (catalog # HM3621) and phalloidin (A22287) was purchased from Life technologies (Grand Island, NY). Anti-Myosin light chain kinase antibody (EP1458Y) was purchased from Abcam (Cambridge, MA). Alexa fluor 647 conjugated anti-Zap70 (pY319) was purchased from BD Bioscience (catalog # 557817). p-Lck (Tyr 394) rabbit polyclonal IgG was purchased from Santa Cruz (catalog # sc-101728). Anti-mouse CD3 epsilon antibody (catalog # 16-0031) was purchased from ebioscience (San Diego, CA). Anti-mouse CD8a blocking antibody (catalog # CL168AP) was purchased from Cedarlane (Burlington, NC). Secondary antibodies, including Alexa fluor 488 goat anti-rat IgG (H+L), Alexa fluor 488 goat anti-rabbit IgG (H+L) and Alexa fluor 647 goat anti-rabbit IgG (H+L), were purchased from Life technologies (Grand Island, NY).

### **MHC**

Biotinylated H-2K(b) monomers were provided by the National Institutes of Health Tetramer Core Facility at Emory University. Monomers are comprised of the designated peptide loaded in the alpha chain of mouse H-2K(b) that is complexed with beta-2-microglobulin (b2m) from either mouse or human origin. In some experiments, the H-2K(b) alpha chain was mutated to prevent the binding of the CD8 co-receptor and these monomers are designated mut to distinguish them from wild type H-2K(b). Specifically, the mouse alpha 3 domain of H-2K(b) was substituted with the alpha 3 domain of human HLA-A2. The peptides folded into the monomers include the cognate chicken ovalbumin 257-264 epitope SIINFEKL (N4) as well as altered forms of the peptide SIIQFEKL (Q4) and SIIVFEKL (V4); more specifically the monomers are designated wild type mouse b2m N4, mut mouse b2m N4, wild type mouse b2m V4 and mouse or human b2m Q4. As a negative control to show specificity, we used the wild type H-2K(b) with human b2m and the GP33-41 epitope of lymphocytic choriomeningitis virus (LCMV).

### OT-1 cell harvesting and purification.

OT-1 T cell receptor transgenic mice were housed and bred in the Division of Animal Resources Facility at Emory University in accordance with the Institutional Animal Care and Use Committee. OT-1 T cells express the CD8 co-receptor and specifically recognize chicken ovalbumin epitope 257–264 (SIINFEKL) in the context of the MHC allele H-2K<sup>b</sup>. Naïve OT-1 T cells were enriched from the spleen using magnetic activated cell sorting according to manufacturer instructions provided with the CD8a+ T cell Isolation Kit (Miltenyi Biotec). Briefly, a single cell suspension of splenocytes was obtained and incubated with biotinylated antibodies specific for unwanted splenic cell populations. These populations were separated from the OT-1 T cells following incubation with anti-biotin magnetic beads and enrichment on a magnetic column. Purified T cells were washed in complete RPMI media [1x RPMI 1640 (Corning), 10% heat-inactivated fetal bovine serum albumin, 10 mM HEPES buffer (Corning), 50mg/mL gentamicin solution (Corning), 5 x 10<sup>-5</sup> M 2-mercaptoethanol and 2 mM L-glutamine (Sigma-Aldrich) and analyzed for purity on the same day.

### DNA sequences

All DNA strands used were custom synthesized and desalted by Integrated DNA Technologies (Coralville, Iowa), except that quencher strand was synthesized by Biosearch technologies (Petaluma, CA) (Table S1).

| Strand ID                           | DNA Sequences (5' to 3')   |
|-------------------------------------|--|
| A21B                                | /5AmMC6/ - CGC ATC TGT GCG GTA TTT CAC TTT - /3Bio/  |
| Quencher                            | /5ThiolMC6-D/ - TTT GCT GGG CTA CGT GGC GCT CTT - /3BHQ_2/   |
| Hairpin (12 pN)                     | GTG AAA TAC CGC ACA GAT GCG TTT <u>GGG TTA ACA TCT</u><br><u>AGA TTC TAT TTT TAG AAT CTA GAT GTT AAC CCT TTA</u><br>AGA GCG CCA CGT AGC CCA GC |
| Hairpin (19 pN)                     | GTG AAA TAC CGC ACA GAT GCG TTT <u>CGC CGC GGG CCG</u><br><u>GCG CGC GGT TTT CCG CGC GCC GGC CCG CGG CGT TTA</u><br>AGA GCG CCA CGT AGC CCA GC |
| Scrambled hairpin                   | GTG AAA TAC CGC ACA GAT GCG TTT <u>ATC GTC AAT ATA</u><br><u>TAC GAT ATT TTT TAG AAT CTA GAT GTT AAC TTT TTA</u><br>AGA GCG CCA CGT AGC CCA GC |
| Complement to the scrambled hairpin | AAA AAG TTA ACA TCT AGA TTC TAA AAA ATA TCG TAT<br>ATA TTG ACG ATA AA  |
| TGT thiol anchor strand             | /5ThiolMC6-D/TTT TTT TTT TCA CAG CAC GGA GGC ACG<br>ACA C  |
| TGT biotin strand (12 pN)           | /5Biosg/GT GTC GTG CCT CCG TGC TGT G   |
| TGT biotin strand (56 pN)           | GT GTC GTG CCT CCG TGC TGT G/3Bio/   |

**Table S1.** DNA sequences. Underscore indicates the stem-loop forming region within hairpins.



**$F_{1/2}$  calculation for 35% GC content hairpin (12 pN).** The following  $F_{1/2}$  calculation was primarily based on the assumptions and measurements used by Woodside et al. (1) The total free energy of the hairpin can be described as follows:

$$\Delta G(F, x) = \Delta G_{fold} + \Delta G_{stretch} + F \times x \quad (\text{eq. 1})$$

, where  $\Delta G_{fold}$  is the free energy of unfolding the hairpin at  $F = 0$ ,  $F$  is the externally exerted force,  $x$  is the hairpin extension and  $\Delta G_{stretch}$  is the free energy of stretching the ssDNA from  $F = 0$  to  $F = F_{1/2}$ , and can be calculated from worm-like chain model as follows:

$$\Delta G_{stretch} = \frac{k_B T}{L_p} \frac{L_0}{4 \left(1 - \frac{x}{L_0}\right)} \left[ 3 \left(\frac{x}{L_0}\right)^2 - 2 \left(\frac{x}{L_0}\right)^3 \right] \quad (\text{eq. 2})$$

where  $L_p$  is the persistence length of ssDNA ( $\sim 1.3$  nm),  $L_0$  is the contour length of ssDNA ( $\sim 0.63$  per nucleotide and  $\sim 27.7$  nm for 44 nucleotides),  $x$  is the hairpin extension from equilibrium and was calculated by using  $(0.44 - (n-1))$  nm, and  $k_B$  is the Boltzmann constant and  $T$  is temperature. To use these equations and estimate the  $F_{1/2}$  for each hairpin probe, we determined the sum of  $\Delta G_{fold}$  and  $\Delta G_{stretch}$ , and estimated the hairpin displacement needed for unfolding,  $\Delta x$ , by using  $((0.44 \times (n - 1)) - 2)$  nm, where  $n$  represents the number of bases comprising the hairpin. Note that we subtract a distance of 2 nm because this corresponds to the initial separation between the hairpin termini, which is set by the diameter of the hairpin stem duplex (effective helix width). When  $F = F_{1/2}$ , then the free energy of the transition equals zero and the  $F_{1/2}$  can be rearranged as follows:

$$F_{1/2} = \frac{(\Delta G_{fold} + \Delta G_{stretch})}{\Delta x} \quad (\text{eq. 3})$$

In our calculations,  $\Delta G_{stretch}$  was determined using equation 2 without modification.  $\Delta G_{fold}$  was determined using nearest neighbour free energy parameters obtained from the IDT oligoanalyzer 3.1, which uses the UNAFold software package. Eq. 3 was used to infer the  $F_{1/2}$  for tension probes at experimental conditions (23 °C, 137.3 mM Na<sup>+</sup> and 0.8 mM Mg<sup>2+</sup>).

| Strand ID       | $\Delta G_{fold}$ (kJ/mol) | $\Delta G_{stretch}$ (kJ/mol) | $\Delta x$ (nm) | $F_{1/2}$ |
|-----------------|----------------------------|-------------------------------|-----------------|-----------|
| Hairpin (12 pN) | 90.83                      | 31.69                         | 16.92           | 12.0      |

**Table S2.**  $F_{1/2}$  calculation for 12 pN DNA probe

$F_{1/2}$  calculation for 100% GC content hairpin (19 pN) is 19.9 pN. However, this hairpin has been experimentally tested and reported (1, 2). The experimental calibration indicates a  $F_{1/2}$  of 19.3 pN. Therefore, we refer to this as the 19 pN hairpin throughout the paper.

**Surface Preparation.** No.2 glass coverslips were rinsed and sonicated with nanopure water ( $18.2 \text{ M } \Omega \text{ cm}^{-1}$ ) for 30 min, and then sonicated with acetone for 15 min. The cleaned slides were then dried in an oven set at 80 °C for 10 min. Fresh piranha solution (7:3 v/v = H<sub>2</sub>SO<sub>4</sub>: H<sub>2</sub>O<sub>2</sub>)

was mixed and then used to clean the substrates for 30 min. Afterwards, the substrates were rinsed with copious amount of nanopure water. The substrates were then sonicated in acetone to remove excess water and to further clean the substrate. Subsequently, 1% v/v APTMS solution in acetone was added to the slides and incubated for 2 h. The amine-modified coverslips were then rinsed in acetone and water and dried under a stream of N<sub>2</sub>.

The slides were then annealed for 1 h at 80 °C. The surface was then passivated with 5% w/v mPEG-NHS (MW 2000) and 0.5% w/v lipoic acid-PEG (MW 3400) in 200 µl of 0.1 M fresh sodium bicarbonate solution. After overnight incubation at 4 °C, the excess unreacted PEG molecules were rinsed with nanopure water. This strategy affords a glass surface with sufficient lipoic acid groups to irreversibly anchor AuNP MTFM sensors at appropriate densities. Finally, coverslips were incubated with 20 nM of unmodified 9 nm AuNP solution for 30 min and then rinsed with nanopure water to remove nonspecifically bound particles.

The DNA tension probe hairpins were assembled in 1X PBS by mixing the Cy3B labeled A21B strand (0.33 µM), quencher strand (0.33 µM) and hairpin strand (0.3µM) in the ratio of 1.1: 1.1: 1. The solution was then heated to 95 °C for 5 min by using a heat block and cooled back to room-temperature over a period of 30 min. Afterwards, an additional 2.7 µM of BHQ2 strands were introduced into the DNA assembly solution in 1 M NaCl. 100 µl of this final solution was added between two AuNP functionalized coverslips and incubated overnight at 4 °C.

DNA tension probe modified coverslips were rinsed in 1X PBS before further functionalization with 40 µg/ml of streptavidin in 1X PBS. After 1 h incubation, the coverslips were rinsed in 1 X PBS to remove the unbound streptavidin, which was followed by the final modification with 40 µg/ml of biotinylated ligands (pMHC or α-CD3) in 1X PBS for 1 h. These modified coverslips were then assembled into cell imaging chambers (Attotfluor, Life Technologies) filled with hank's balanced salt imaging buffer and immediately used for cell experiments.

In the case of tension gauge tether (TGT), a 75 x 25 mm glass slide was cleaned and functionalized with amine groups using the aforementioned method. A 6 channel µ-Slide was then mounted to the glass slide to create 6 well flow chambers, which was then passivated with 5% w/v mPEG-NHS (MW 2000) and 0.5% w/v lipoic acid-PEG (MW 3400) in 0.1 M fresh sodium bicarbonate solution at 4 °C for overnight. Surfaces were washed extensively with nanopure water and then 20 nM AuNP solution was introduced and incubated for 30 min. After thorough rinsing, the hybridized TGTs were dissolved in 1 M sodium chloride solution and were incubated overnight at 4 °C with 10 µM of HS-(CH<sub>2</sub>)<sub>11</sub>-(OCH<sub>2</sub>CH<sub>2</sub>)<sub>6</sub>-OCH<sub>3</sub> passivating polyethylene glycol. Excess DNA and PEG were removed with three washes of 1X PBS. Afterwards, 40 µg/mL of streptavidin was added and incubated for 1 h. The surfaces were then washed with 1X PBS and subsequently 40 µg/ml of biotinylated ligands (pMHC or α-CD3) was added and allowed to bind to the streptavidin modified duplexes for 1 h. Unbound ligand was washed away with 1X PBS and the surfaces were used within the same day of preparation.

**Bulk fluorescence measurement.** The fluorescence intensity of Cy3B was recorded using a Biotek Synergy HT plate reader operated using a filter set with excitation/emission λ = 565 nm/610 nm. Each well in the 96-well plate (Fisher scientific) was filled to a volume of 100 µl.

All measurements were performed in triplicate, and the reported error bars represent the standard deviation of these measurements.

**HPLC.** Reaction products were purified using a C18 column (diameter: 4.6 mm; length: 250 mm) in a reverse phase binary pump HPLC that was coupled to a diode array detector (Agilent 1100).

**MALDI-mass spectrometry.** Concentration of the purified oligonucleotide conjugate was determined by measuring its  $A_{260}$  value on Nanodrop 2000 UV-Vis Spectrophotometer (Thermo Scientific). MALDI-TOF mass spectrometry was performed on a high performance MALDI time-of-flight mass spectrometer (Voyager STR). The matrix for all experiments was prepared by freshly dissolving excess of 3-hydroxypicolinic acid (3-HPA) in the matrix solvent (50% MeCN/H<sub>2</sub>O, 1% TFA, 10% of 50 mg/ml ammonium citrate).

**Calcium imaging.** Freshly purified OT1 cells ( $n = 1 \times 10^6$ ) were centrifuged to remove the RPMI media and re-suspended in 3 ml of hank's imaging buffer. 10  $\mu$ l of 1 mM of fura-2/Am in DMSO was added into the cell suspension. The mixture solution was kept at 37 °C for 30 min. Afterwards, cells were pelleted by centrifugation at 1200 rpm for 4 min and re-suspended in 3 ml of imaging buffer for additional 15 min incubation. This step is to ensure full de-esterification of the fura-2/Am. Then, the cells were again pelleted in previous described condition and re-suspended in 1 ml of imaging buffer and prepared for seeding.

Nikon CFI S Fluor 100x oil objective, a Chroma 340 excitation filter set (ET340x, T400lp and ET510/80m) and Chroma 380 excitation filter set (ET380x, T400lp and ET510/80m) was used to image and quantify the 510 nm fluorescence intensity with excitation at both 340 nm and 380 nm of fura-2 dye. During an experiment, the fluorescence images were acquired by using 340 and 380 filter sets sequentially. Afterwards, ImageJ was used to generate a cell mask for both channels excited by 340 nm and 380 nm. Final fura-2 ratio ( $I_{340}/I_{380}$ ) was calculated by using the image calculator function in ImageJ.

**Fluorescence immunostaining.** Naïve OT1 cells were seeded onto the tension probe surfaces decorated with different stimulatory ligands. After cell spreading and activation, 4% of paraformaldehyde was gently added to the imaging chamber for 30 min. After thoroughly rinsing with 1X PBS, 0.1% Triton-X was added to the chamber for 10 min. Subsequently, 1X PBS was used to rinse the chamber, which is followed by 2% w/v BSA passivation for 24 h at 4 °C. Without rinsing, primary antibody was directly added into the chamber for targeting the protein of interests and incubate for 1 h at room temperature. Optionally, fluorescently labeled secondary antibody was also added and incubated for 1 h for visualization when primary antibody was not labeled. The standard manufacture recommended concentrations and conditions were used for immunostaining.

**Drug Inhibition.** For Lck inhibition, 30  $\mu$ M of Lck inhibitor was incubated with OT1 cells either before or after cell plating. In probing cytoskeletal activities, 40  $\mu$ M ROCK inhibitor (Y-27632), 40  $\mu$ M MLCK inhibitor (ML-7), 20  $\mu$ M F-actin inhibitor (Cytochalasin D), 50  $\mu$ M Arp2/3 inhibitor (CK-666) was added after 30 min cell plating, respectively. In probing GTPase activities, 200  $\mu$ M Rac1 inhibitor (NSC23766) and 10  $\mu$ M Cdc42 inhibitor (ML141) was

pretreated with freshly purified OT1 cells ( $n = 1 \times 10^6$ ), respectively, for 30 min before cell plating.

**AFM imaging.** The density of AuNP tension sensor on the functionalized glass coverslip was measured by using an atomic force microscope mounted on an anti-vibration stage (MFP-3D, Asylum Research, CA). Silicon AFM tips (MikroMasch) with a force constant (5.4-16 N/m) were used to image the sample in tapping mode at a scan rate of 1 Hz. All images were processed and rendered using IgorPro.



## **Supplementary movie captions**

### **Movie S1. Simultaneous imaging of TCR tension generation and T cell activation**

Timelapse video showing a naïve OT1 cell pre-treated with fura-2 ratiometric dye plated on a 19 pN tension probe substrate presenting  $\alpha$ -CD3. The video was 10 min long. The RICM channel (left), TCR tension channel (middle) and fura-2 ratio channel (right) are shown side by side.

### **Movie S2. ML-7 leads to the shrinkage of cell-surface contact and condensation of tension**

Timelapse video showing naïve OT1 cells plated on a 12 pN tension probe substrate presenting N4 pMHC upon treatment with 40  $\mu$ M of ML7.  $t = 0$  min represents the time at which ML7 was added. Brightfield, RICM, TCR tension, and merged channel from RICM and tension are shown from left to right.

### **Movie S3. TCR tension dynamics in response to pMHC stimulation**

Timelapse video of naïve OT1 cells plated on a 12 pN tension probe substrate presenting N4 pMHC. The timelapse movie was captured from  $t = 0$  min to  $t = 34$  min to show the spatiotemporal dynamics of TCR tension upon cell-substrate contact. RICM, TCR tension, and merged channel from RICM and tension are shown from left to right.

### **Movie S4. Cell migration and tension dynamics in response to the copresentation of pMHC/ICAM-1**

Timelapse video of naïve OT1 cells plated on a 19 pN tension probe substrate co-presenting N4 pMHC and ICAM-1 ligands 15 min after plating. The timelapse movie was captured for 10 min to show the migratory behavior of T cells and characteristic TCR tension at the trailing edge. The interval between each frame is 30 s. Brightfield (top left), RICM (top right), TCR tension (bottom left), and merged channel from RICM and tension (bottom right) are shown in a quadrant.

### **Movie S5. OT-1 Cell tension dynamics and $[Ca^{2+}]$ flux in response to the V4 ligand**

Timelapse video of naïve OT1 cells pre-treated with fura-2 ratiometric dye plated on 12 pN tension probe substrate presenting V4 pMHC. The timelapse movie was ~10 min long. The RICM channel (left), TCR tension channel (middle) and fura-2 ratio channel (right) are shown side by side. Normalized fura-2 ratio was colored coded representing the value from 1.0 to 2.0.

### **Movie S6. OT-1 Cell tension dynamics and $[Ca^{2+}]$ flux in response to the N4 ligand**

Timelapse video of naïve OT1 cells pre-treated with fura-2 ratiometric dye plated on 12 pN tension probe substrate presenting N4 pMHC. The timelapse movie was ~6 min long. The RICM channel (left), TCR tension channel (middle) and fura-2 ratio channel (right) are shown side by side. Normalized fura-2 ratio was colored coded representing the value from 1.0 to 5.0.

## Supplementary Note 1

The DNA-based nanoparticle tension probes displayed a 103-fold increase in fluorescence increase upon unfolding (Fig. 1B). Based on AFM analysis, the density of gold nanoparticles sensors is approximately 11 AuNPs per EMCCD pixel area (160 nm  $\times$  160 nm). Bulk fluorescence measurements indicate that an average of 4.4 DNA hairpins are bound per AuNP. Given that the maximum fluorescence signal associated with the fully opened hairpin sensors is 37900 a.u. per pixel, we estimate that each activated tension sensor contributes a value of 783 a.u. in fluorescence. This analysis indicates that a minimum of  $\sim 31$  DNA hairpins ( $F_{1/2} = 19$  pN) are mechanically unfolded per  $\mu\text{m}^2$  based on the  $\alpha\text{CD3}$  stimulation data shown in Fig. 2E. Note that only a subset of bound TCR molecules transmit mechanical forces sufficient to unfold the DNA hairpins. In principle, these AuNP-DNA based tension probes provide sufficient sensitivity for single molecule detection.

## Supplementary Note 2

All the DNA tension probes used in this study are either experimentally calibrated (19 pN) using single molecule spectroscopy methods (1, 2) or theoretically calculated based on literature precedent for the  $F_{1/2} = 12$  pN at 23  $^{\circ}\text{C}$  (see Table S2 in SI methods). Therefore, T cell experiments were performed at the room temperature rather than 37  $^{\circ}\text{C}$ . We acknowledge that this temperature choice may lead to suboptimal cell activity such as delayed calcium flux. Nonetheless, we observed significant phosphorylation of Lck and Zap70 within a few minutes following cell seeding (Fig. 2C), which is in agreement with the rates of T cell activation in other reported work (3). This suggests that T cell response is not compromised in our experimental conditions.

In experiments using TGTs to physically limit the maximum TCR-pMHC force, we cultured T-cells at 37  $^{\circ}\text{C}$  for 30 min prior to cell fixation and staining. This is because TGT tension tolerance values for both the 12 and 56 pN probes were previously calculated at 37  $^{\circ}\text{C}$  (4). Moreover, the 12 and 56 pN TGT probes were selected based on the tension sensor results shown in Fig. 2A and E. The 56 pN probe is expected to provide the most mechanically stable tether, and thus remain hybridized to the surface resisting TCR forces that exceed  $\sim 19$  pN. In contrast, the 12 pN TGT probes provide a labile tether that is expected to dissociate in response to TCR forces exceeding 12 pN. Thus, these two TGTs cap TCR forces at the most relevant critical thresholds of tension.

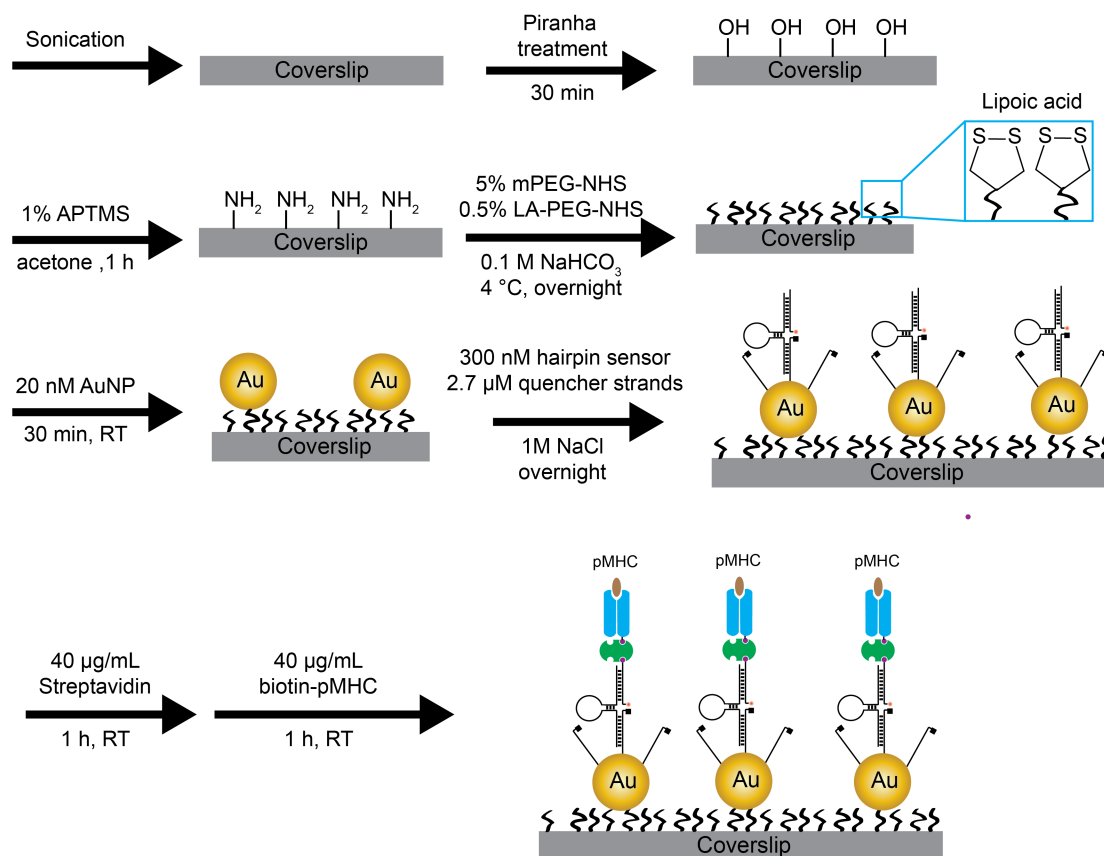


**Fig. S1. Fabrication of DNA-based gold nanoparticle tension sensor surface.** Flow chart showing the step-wise fabrication of DNA-based gold nanoparticle tension probes (see methods for full description).

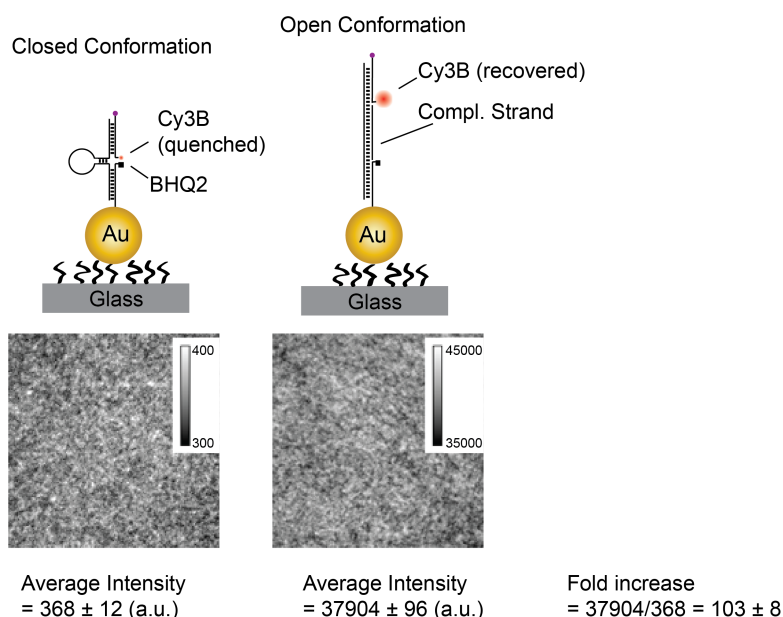


**Fig. S2. Quenching efficiency calibration of DNA-AuNP tension probes.** Scheme and representative images of the experiments used to determine the quenching efficiency of DNA tension probes on the AuNP surface. The closed conformation probe sample was prepared as described in the Fig. S1. The open conformation probe used a complementary strand to the scrambled hairpin at  $0.3 \mu\text{M}$  (for sequences see Table 1 in methods section). This complementary strand generated a duplex, thus separating the dye from AuNP surface and the molecular quencher. This approach was adapted from energy transfer efficiency calibration experiments reported previously (5, 6). The calculated fold increase is  $103 \pm 8$ .



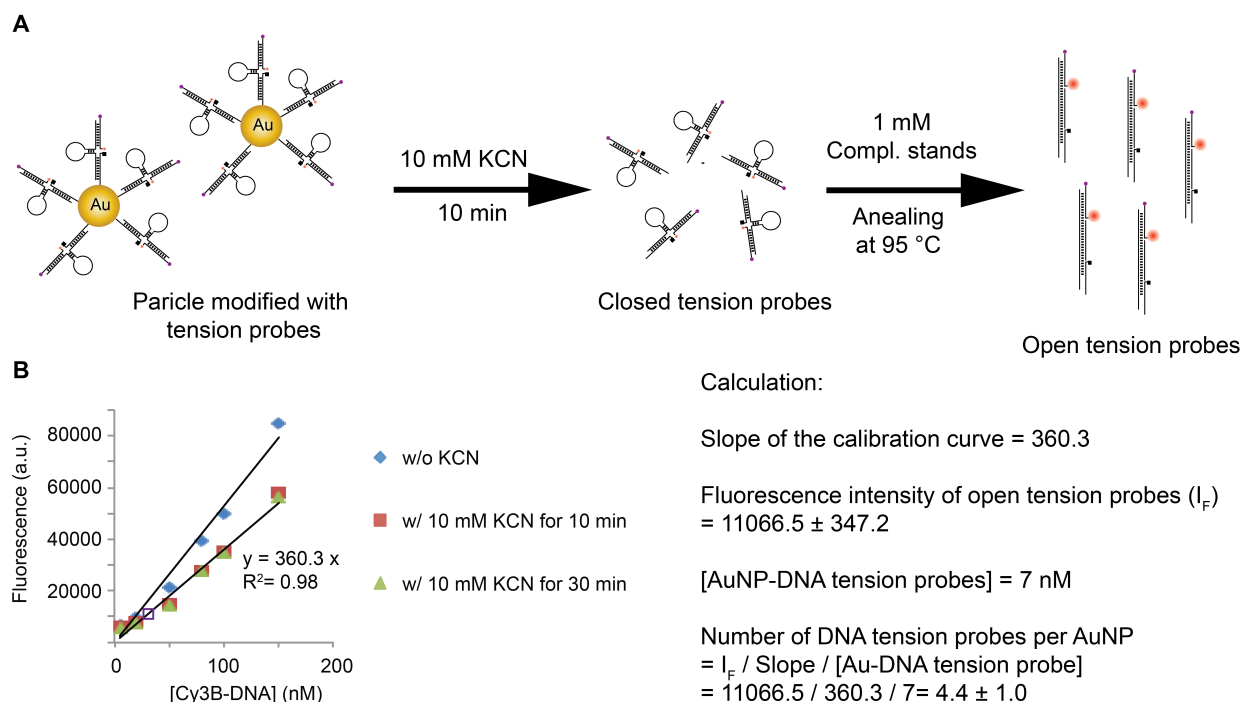


**Fig. S3. Quantification of the average number of DNA sensors per gold nanoparticle.** (A) Scheme showing the approach used to determine the average stoichiometry between Cy3B-labeled tension probes and AuNP. Briefly, the concentration of AuNP was determined from the absorbance at  $\lambda=520$  nm. Subsequently, AuNPs were dissolved by treating the sample with 10 mM KCN, which released Cy3B-labeled tension probes within 10 min. 1 mM of complementary DNA was then added into the solution and heated up to 95°C for hybridization and opening of the hairpin. The fluorescence intensity of the released Cy3B dye was then used to determine the number of dye molecules in the sample. (B) Plots showing the calibration curve used to quantify the number of tension sensor ligands per AuNP. The blue diamonds represent the calibration curve for Cy3B without addition of KCN. The red squares and green triangles represent the calibration curve at different time points with KCN, while the purple box represents the sample containing the released Cy3B ligands from AuNP-tension probes. All measurements were performed in triplicate.

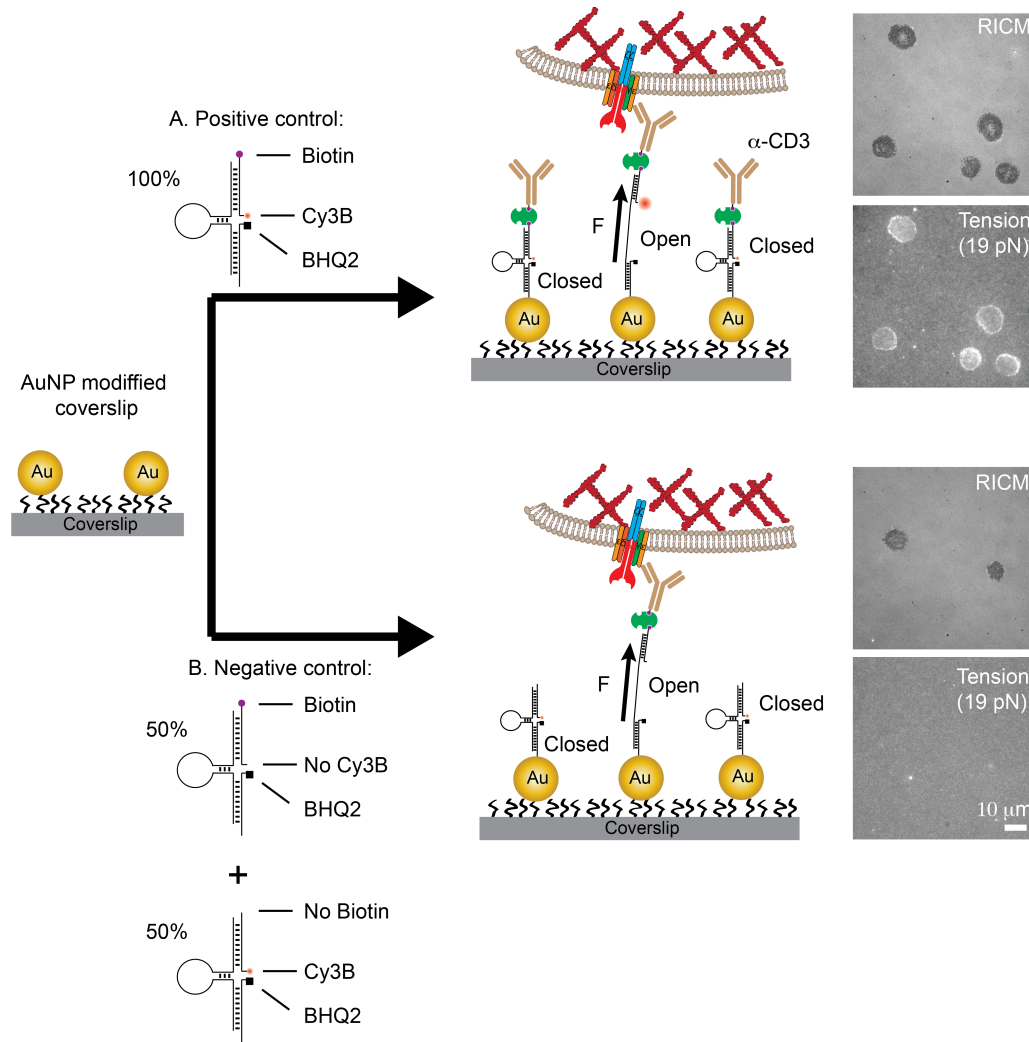


**Fig. S4. Tension signals are specifically generated through TCR-ligand interactions.** (A) Schematic representation of the procedure used to generate the positive control sample containing the DNA-based AuNP tension probes modified with  $\alpha$ -CD3. The images show representative RCM and 19 pN tension signal for OT-1 cells cultured on the surface for 15 min. (B) Schematic representation of procedure used to generate the negative control sample which included AuNP modified with two types of hairpins at equal concentration. The first hairpin incorporated the Cy3B dye-BHQ2 quencher pair but lacked the biotin group at the terminus of the A21B strand. The second hairpin incorporated the biotin group but lacked the Cy3B dye on the A21B strand. Cell spread on these substrates. However, no detectable fluorescence signal was observed, showing that only specific interaction between TCR and its ligand leads to tension signal.

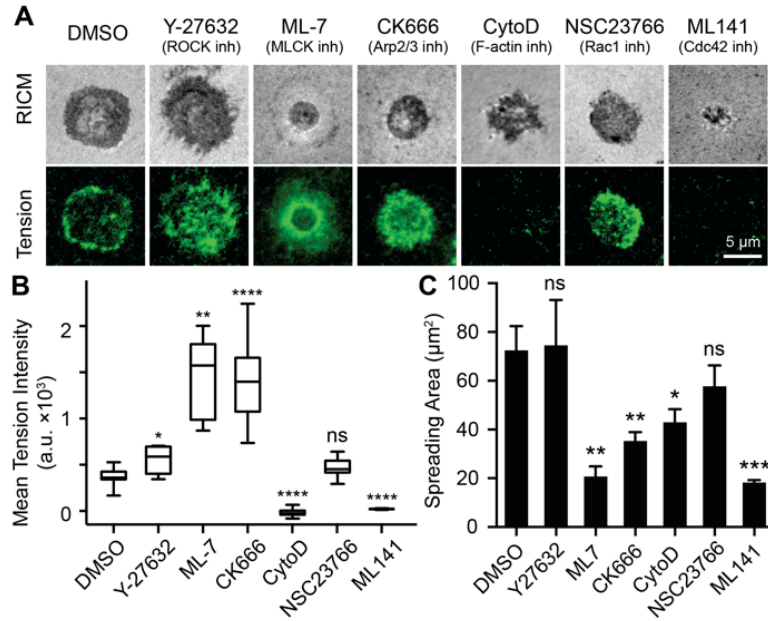


**Fig. S5. Investigation of cytoskeletal elements mediating TCR forces.** (A) Representative RICM and 19 pN TCR tension images of T cell treated with different cytoskeletal inhibitors. (B-C) Statistical analysis of 19 pN TCR tension (B) and cell spreading area (C) for T cells treated with different cytoskeletal inhibitors ( $n = 20$  cells for each condition). All error bars represent s.d., \* $P$ -value  $< 0.1$ ; \*\* $P < 0.01$ ; \*\*\* $P < 0.001$  and \*\*\*\* $P < 0.0001$ .

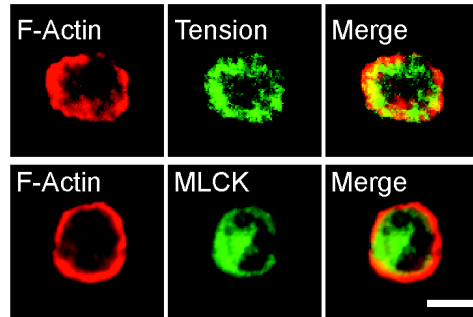


**Fig. S6. Colocalization of TCR tension with F-actin, and F-actin colocalization with myosin light chain kinase.** Representative immunostaining images of OT1 cells showing the colocalization between TCR tension (19 pN) and F-Actin assembly (top row) and F-actin colocalization with MLCK (bottom row). In general, F-actin and tension were highly colocalized, while we observed a spatial offset between the F-actin structure and the MLCK at the cell edge. Scale bar: 10  $\mu\text{m}$ .



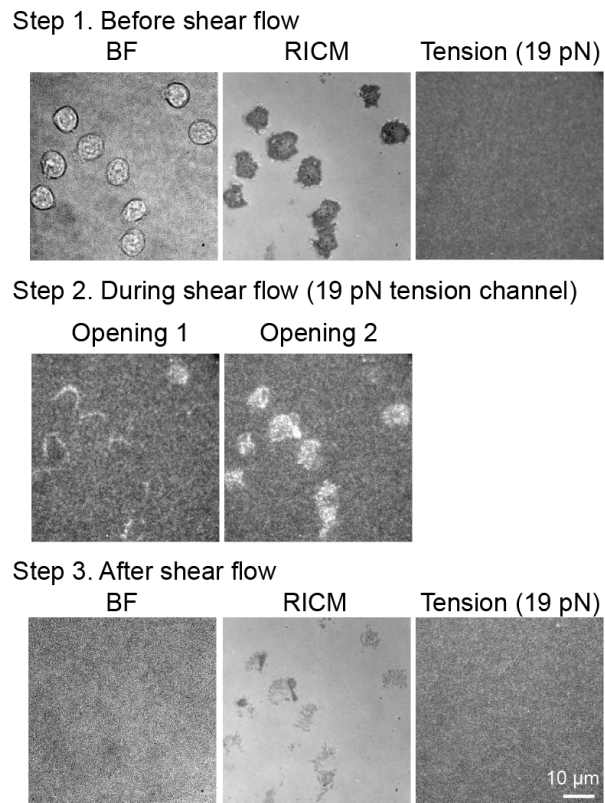


**Fig. S7. Induction of 19 pN sensor by shear flow.** Representative images showing that OT1 cells spread and generated no observable tension signals when they were plated onto the N4 decorated 19 pN tension probe surface (step 1). A strong shear flow was generated by pipetting a stream of imaging buffer into the cell chamber, which led to a step-wise increase in fluorescence intensity both at the edge and center (step 2). Eventually, the cells were removed from the surface (RICM) and tension probes recovered back to background levels (step 3).

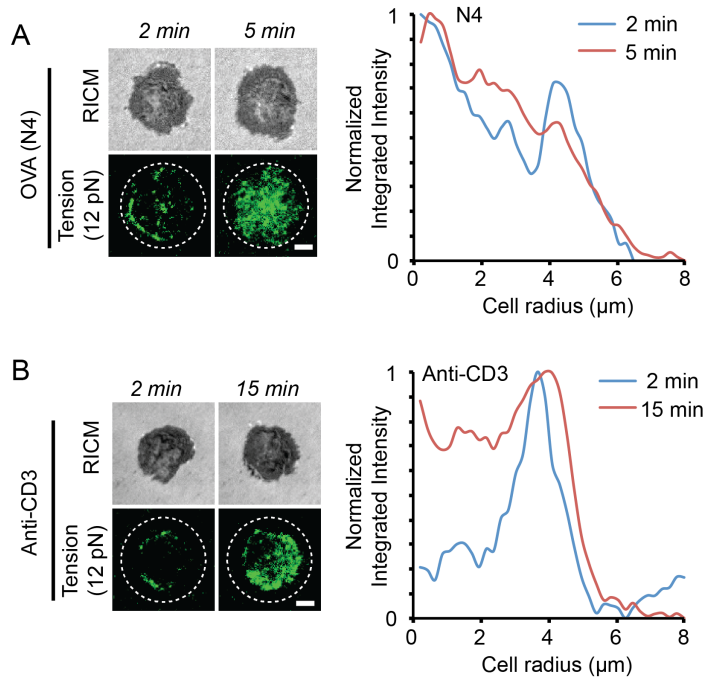


**Fig. S8. Radial distribution function analysis of TCR tension upon ligand stimulation.** (A) Representative RISM and 12 pN TCR tension images for OT-1 cells plated onto the N4 pMHC 2 and 5 min after cell-surface contact. The dotted circle represents the ROI used for radial distribution analysis using radial profile plugin in ImageJ. Plots show cell radius ( $r$ ) vs fluorescence intensity for this cell at  $t = 2$  min and 5 min following cell-surface contact. Analysis of tension at  $t = 2$  min showed that forces were generally concentrated in a ring-like structure at the cell periphery. However, a peak at  $t = 4$ -5 min was observed in the central area. (B) Representative RISM and 12 pN TCR tension images for OT-1 cells plated onto the  $\alpha$ -CD3 2 and 15 min after cell-surface contact. TCR tension at  $t = 2$  min were concentrated in a ring-like structure. The characteristic ring-like structure was maintained for 15-60 min. Scale bar: 3  $\mu\text{m}$ .

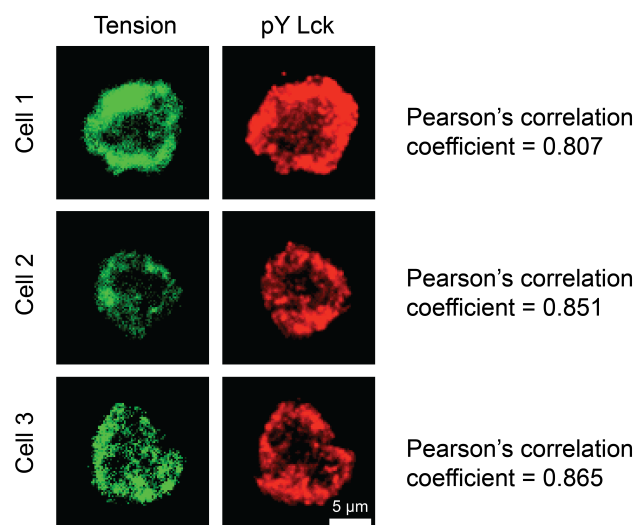


**Fig. S9. Spatial correlation analysis between TCR tension and active Lck.** Representative images of 19 pN TCR tension and phosphorylated Lck (pY394). Pearson's correlation coefficients were analyzed using the JACoP plugin implemented in Fiji. Briefly, individual cells acquired from each fluorescence channel were fed into the JACoP plugin, and the result of this analysis are reported here.  $n = 20$  cells from 3 different chambers were analyzed and an average coefficient of  $0.84 \pm 0.04$  was reported here.

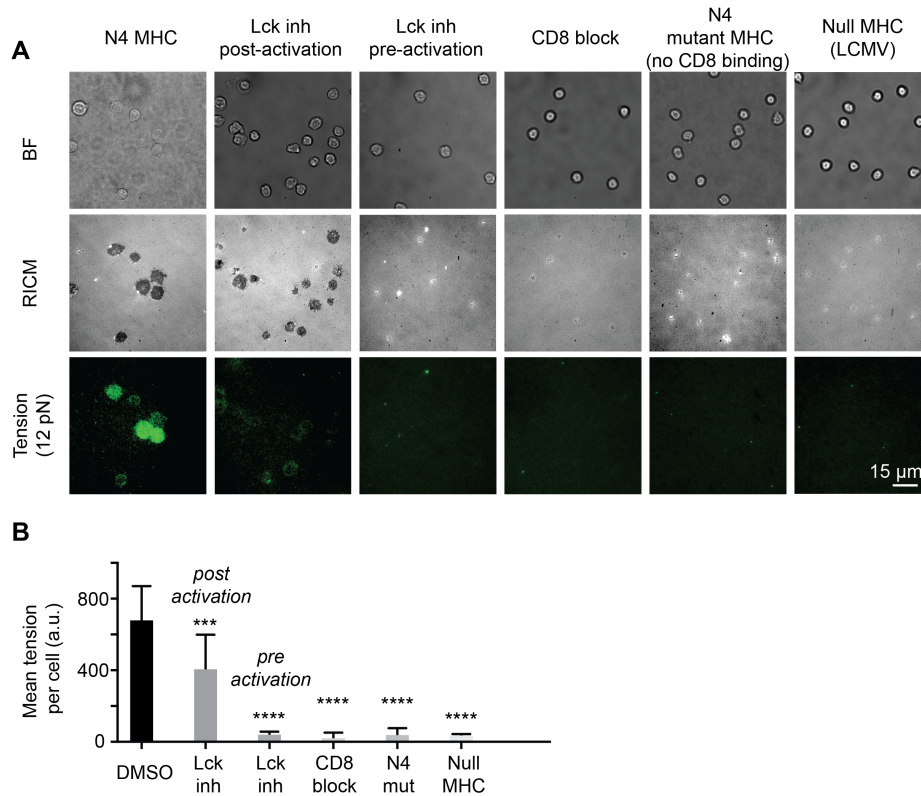


**Fig. S10. Quantification of TCR tension upon perturbation of TCR, CD8 and Lck activities.** (A) Representative brightfield, RICM and tension images showing differential T cell responses to different Lck inhibitors before (pre-activation) and after (post-activation) cell plating, CD8 blocking with antibody, mutant N4 pMHC with abolished CD8 binding, and null pMHC presenting the GP33-41 epitope from LCMV. (B) Bar graph quantifying the mean fluorescence tension signal per cell in responses to treatments described in (A). Error bars represent the standard deviation (S.D.) from  $n = 20$  cells for each group. \*\*\* $P < 0.001$  and \*\*\*\* $P < 0.0001$ .



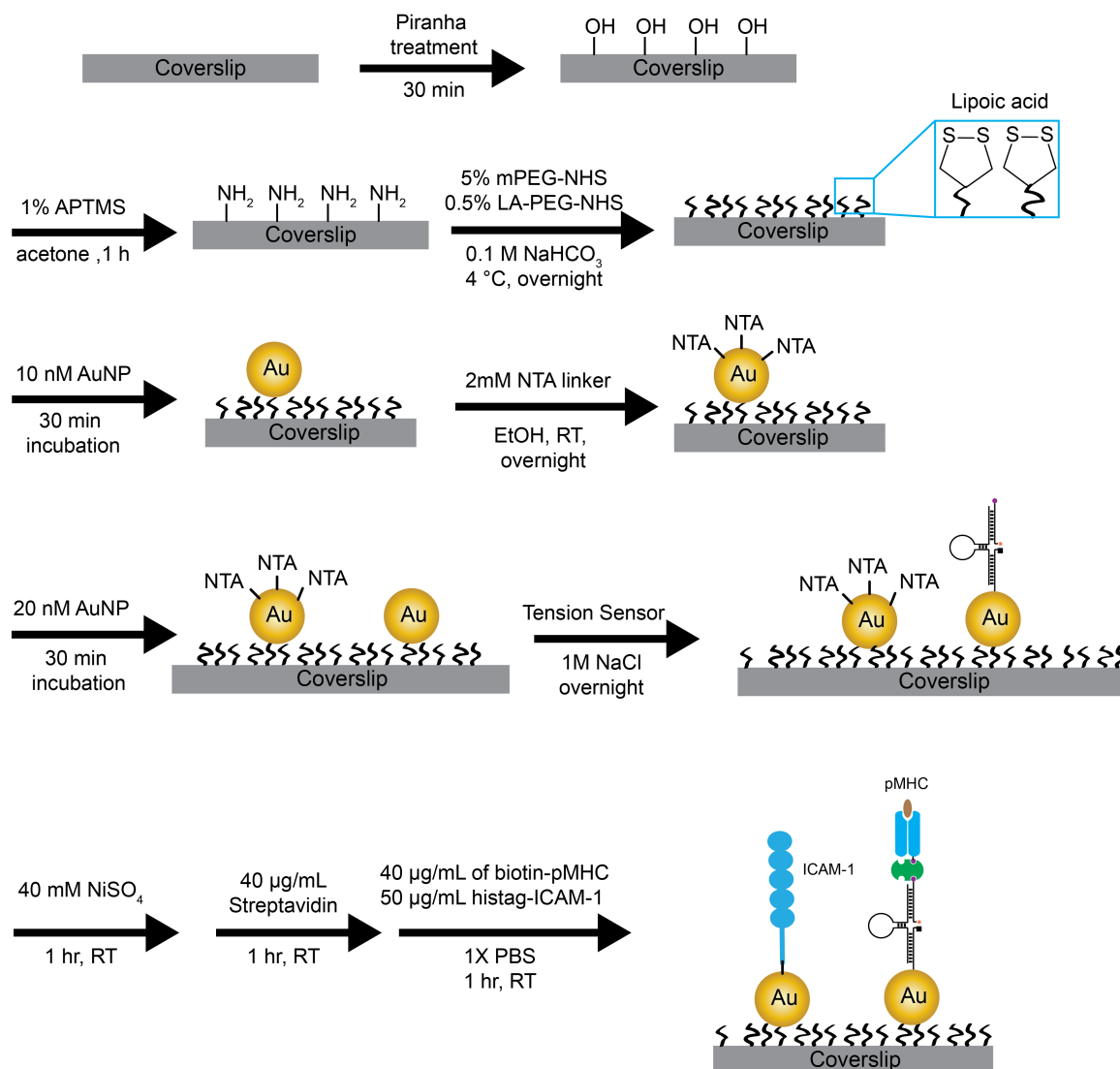


**Fig. S11. Co-presentation of ICAM-1 and DNA tension sensor-pMHC ligands on AuNP.** Flow chart showing the step-wise fabrication of AuNP surfaces co-presenting ICAM-1 and DNA tension sensor-pMHC ligands.

No.2 glass coverslips were rinsed and sonicated with nanopure water ( $18.2 \text{ M}\Omega \text{ cm}^{-1}$ ) for 30 min, and then sonicated twice with acetone for 15 min. The slides were then dried in an oven set at  $80^\circ\text{C}$  for 10 min. Fresh piranha solution ( $7:3 \text{ v/v} = \text{H}_2\text{SO}_4: \text{H}_2\text{O}_2$ ) was mixed and then used to clean the substrates for 30 min. Afterwards, the substrates were rinsed with a copious amount of nanopure water. The substrates were then sonicated in acetone to remove excess water and for further cleaning. Subsequently, 1% v/v APTMS solution in acetone was added to the slides and incubated for 2 h. The amine-modified coverslips were then rinsed in acetone and water and dried under stream of  $\text{N}_2$ .

The slides were then annealed for 1 h at  $80^\circ\text{C}$ . The surface was then passivated with 5% w/v mPEG-NHS (MW 2000) and 0.5% w/v lipoic acid-PEG (MW 3400) in 200  $\mu\text{l}$  of 0.1 M fresh

sodium bicarbonate solution. After overnight incubation at 4 °C, the excess unreacted PEG molecules were rinsed with nanopure water. This strategy affords a glass surface with sufficient lipoic acid groups to irreversibly anchor AuNP MTFM sensors at appropriate densities. Next, 10 nM of unmodified 9 nm AuNP solution was incubated for 30 min and then rinsed with nanopure water to remove nonspecifically bound particles.

400 µl of 2 mM of NTA-SAM reagent in pure ethanol was incubated with the AuNP modified coverslips overnight at RT. The coverslips were then placed in a petri dish containing pure ethanol to prevent sample from drying. After rinsing with copious ethanol, the coverslips were air-dried and incubated with 40 mM of NiSO<sub>4</sub> solution for 1 h. Afterwards, an additional 20 nM solution of unmodified AuNPs was incubated with the coverslip for 30 min before modification of tension probes.

The DNA tension probe hairpins were assembled in 1X PBS by mixing the Cy3B labeled A21B strand (0.33 µM), quencher strand (0.33 µM) and hairpin strand (0.3 µM) in the ratio of 1.1: 1.1: 1. The solution was then heated to 95 °C for 5 min by using a heat block and cooled back to room-temperature over a period of 30 min. Afterwards, an additional 2.7 µM of BHQ2 strands were introduced into the DNA assembly solution in 1 M NaCl. 100 µl of this final solution was added between two AuNP functionalized coverslips and incubated overnight at 4°C.

DNA tension probe modified coverslips were rinsed in 1X PBS before further functionalization with 40 µg/ml of streptavidin in 1X PBS. After 1 h incubation, the coverslips were rinsed in 1 X PBS to remove the unbound streptavidin, which was followed by the final modification with a mixture of 40 µg/ml of biotinylated ligands (pMHC or α-CD3) and 50 µg/ml of histag-ICAM-1 in 1X PBS for 1 h.

These modified coverslips were then assembled into cell imaging chambers (Attofluor, Life Technologies) filled with hank's balanced salt imaging buffer and immediately used for cell experiments.

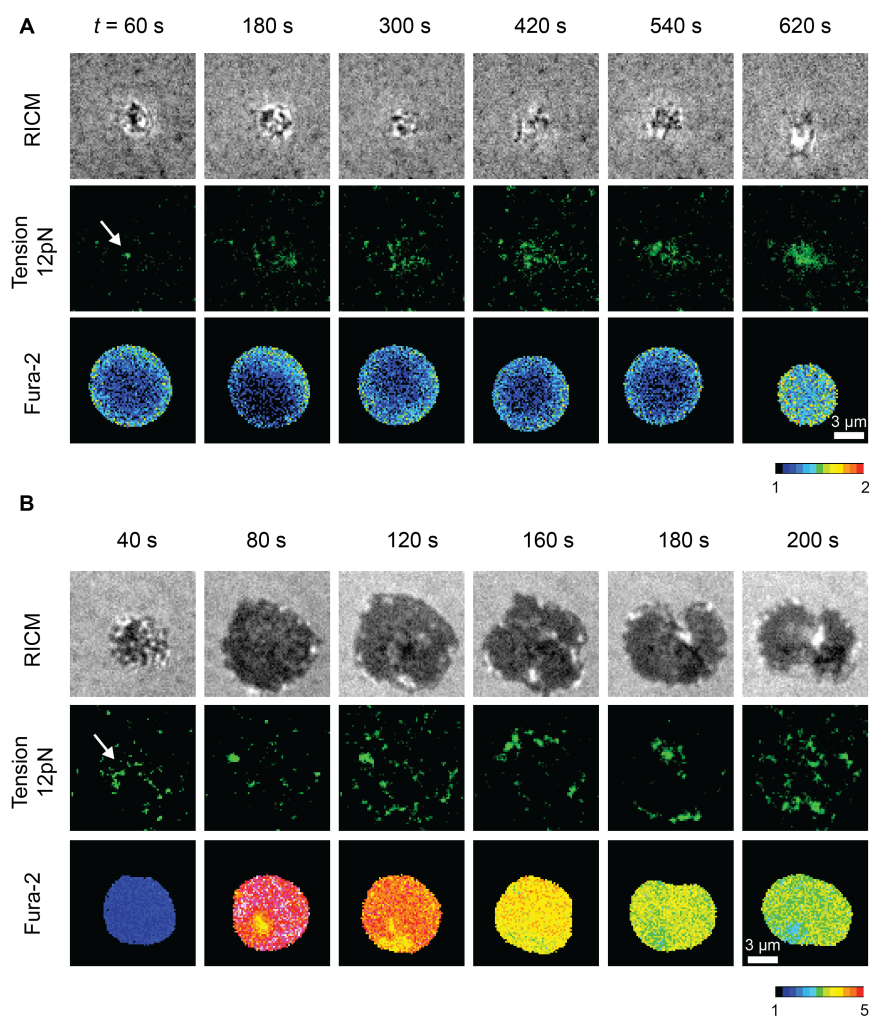


**Fig. S12. Comparison of TCR forces and calcium flux between V4 and N4 ligand.** Simultaneous imaging of cell spreading (Reflection interference contrast microscopy, RICM), 12 pN TCR forces (tension) and T cell activation (fura-2) for a representative OT-1 cell encountering V4 pMHC (A) and N4 pMHC (B). White arrow indicates the initial appearance of tension signals within 1 min of cell-substrate contact.

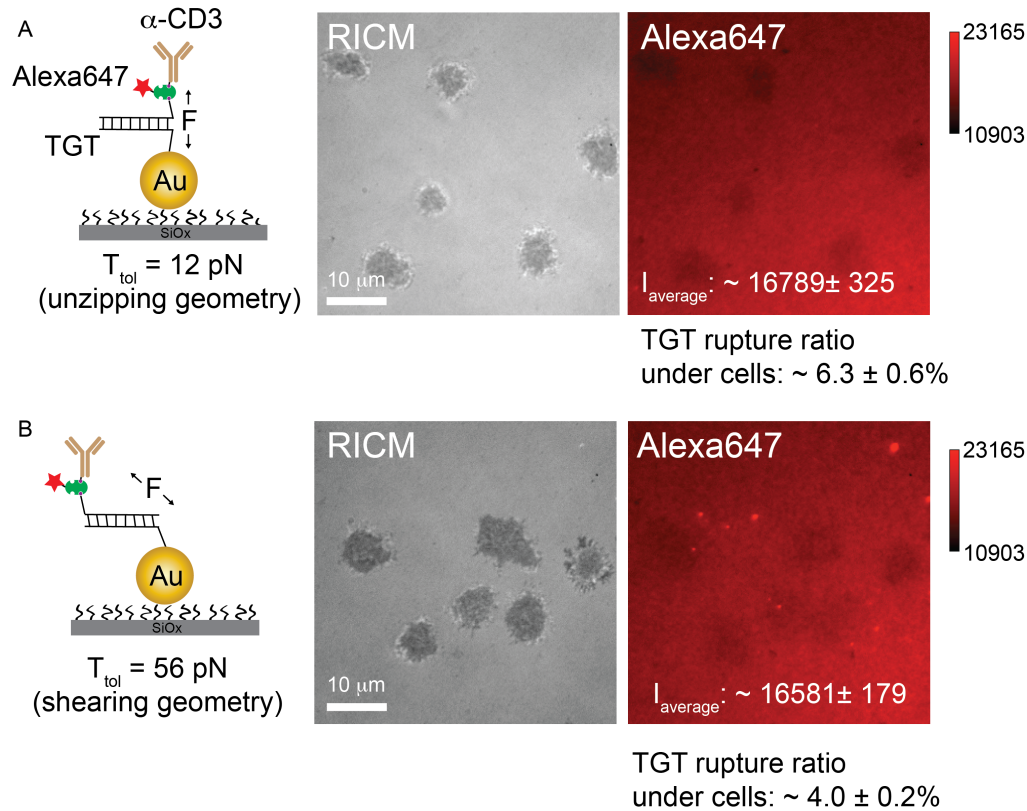


**Fig. S13. Comparison of TGT rupturing between 12 pN and 56 pN probes.** (A) Schematic representation of 12 pN TGT modified with  $\alpha$ -CD3. RICM and fluorescence images show the result of T cells cultured on this surface for 30 min. T cells spread and generated mechanical forces that dissociate the TGT duplex, leaving an area with decreased fluorescence intensity. Quantification analysis showed a  $6.3 \pm 0.6\%$  decrease in fluorescence due to DNA rupturing. (B) Schematic representation of 56 pN TGT modified with  $\alpha$ -CD3. Upon plating, OT1 cells spread and generated mechanical forces that reduced the streptavidin intensity by  $4.0 \pm 0.2\%$ . These results confirmed the model that 56 pN TGT provided greater mechanical resistance than the 12 pN TGT.  $n = 20$  cells were analyzed.

## References

1. Woodside MT, *et al.* (2006) Nanomechanical measurements of the sequence-dependent folding landscapes of single nucleic acid hairpins. *Proc Natl Acad Sci USA* 103(16):6190-6195.
2. Blakely BL, *et al.* (2014) A DNA-based molecular probe for optically reporting cellular traction forces. *Nat Methods* 11:1229-1232.
3. Yokosuka T, *et al.* (2005) Newly generated T cell receptor microclusters initiate and sustain T cell activation by recruitment of Zap70 and SLP-76. *Nat Immunol* 6(12):1253-1262.
4. Wang XF & Ha T (2013) Defining Single Molecular Forces Required to Activate Integrin and Notch Signaling. *Science* 340(6135):991-994.
5. Liu Y, Yehl K, Narui Y, & Salaita K (2013) Tension Sensing Nanoparticles for Mechano-Imaging at the Living/Nonliving Interface. *J Am Chem Soc* 135(14):5320-5323.
6. Jennings T, Singh M, & Strouse G (2006) Fluorescent lifetime quenching near  $d = 1.5$  nm gold nanoparticles: probing NSET validity. *J Am Chem Soc* 128(16):5462-5467.